Metal–Support Interactions in Pt-WO 3 Heterostructures: Role of WO 3 Polymorphism

Isabel Gómez-Recio, Cyril Thomas, Christophe Méthivier, María Luisa Ruiz-González, José González-Calbet, David Portehault

Metal–Support Interactions in Pt-WO_3 Heterostructures: Role of WO_3 Polymorphism

Isabel Gómez-Recio,[⊥] Cyril Thomas,[⊥] Christophe Méthivier, María Luisa Ruiz-González, José M. González-Calbet,* and David Portehault*

ABSTRACT: Ionic exchange under soft conditions yields nanoplatelets of tungsten bronzes with an original crystal structure doped with cobalt, copper, platinum, and cesium cations (h'-M_xWO_3). The optimal orientation of the tunnel-based crystal structure, perpendicular to the basal plane of the nanoplatelets, facilitates cation exchange so that the dopant cations are located inside the $(WO_6)_6$ channels, as evidenced by scanning transmission electron microscopy and electron energy loss spectroscopy. This synthetic pathway allows one to obtain not only doped materials but also metallic nanoparticles supported over h'-WO_3 nanoplatelets after reduction. Consequently, this approach opens a route to target new hexagonal bronze compositions. We have used this approach to design Pt nanoparticles supported over the two known hexagonal WO_3 polymorphs: h'-WO_3 and h-WO_3. By using the catalysis of CO oxidation as a probe, we highlight differences in the metal–support interaction on these Pt-WO_3 heterostructures, especially higher electron transfer from the newly discovered h'-WO_3 framework.

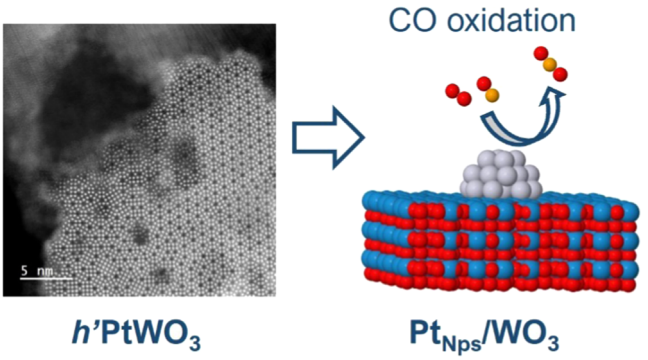

INTRODUCTION

Octahedral molecular sieves (OMSs) are oxides with tunnels in their structure due to the arrangement of MO_6 octahedra. These channels can exchange ions and/or water molecules with the local environment of the materials. This exchange can be reversible without alteration of the oxide host structure. Cation exchange in OMSs affords the possibility to adjust many features, such as metal oxidation state, electrical conductivity, and surface acidity.[1,2] As a consequence, the OMS materials exhibit tunable properties for implementation in many chemical processes. Among OMS materials, zeolites and manganese oxides have been extensively studied,[3−6] but other elements, such as tungsten, can also adopt such structures. When the channels are at least partially filled, tungsten OMSs are called bronzes.[7−9]

Tungsten bronzes have the general formula M_xWO_3, where M^{n+} cations are incorporated into the WO_3 channels. In hexagonal bronzes, these cations are primarily located inside the hexagonal tunnels formed by six WO_6 octahedra sharing corners (Figure 1).[2] Occasionally, smaller tunnels, made up of four or three interconnected octahedra, can also host additional cations.[9−12] Presently, two different hexagonal polymorphs of WO_3, h-WO_3, and h'-WO_3 (Figure 1),[12] differing in the arrangement of the octahedral units connecting the hexagonal tunnels, have been described. The latter, h'-WO_3 framework, has been recently reported.[2] Hexagonal tungsten bronzes reported to date are mostly referred to as the h form, while bronzes with the h' framework have been reported only for protons inserted in the channels.[12]

The relatively large channels of the h'-WO_3 hexagonal structure (5.1 Å) should enable hosting various cations, like in the h-WO_3 framework.[1,10,13] This characteristic makes them potential candidates in applications based on ion intercalation/deintercalation processes, such as electrochromic devices where ion intercalation leads to tungsten reduction and then optical absorption modification. The h'-WO_3 structure can only be obtained as nanostructures, which sets favorable conditions for ion exchange, as suggested by shortened intercalation paths and superior tunnel accessibility that enhance coloration efficiency and switching speed, in comparison with bulk materials.[1,11,14] Modifying the nature

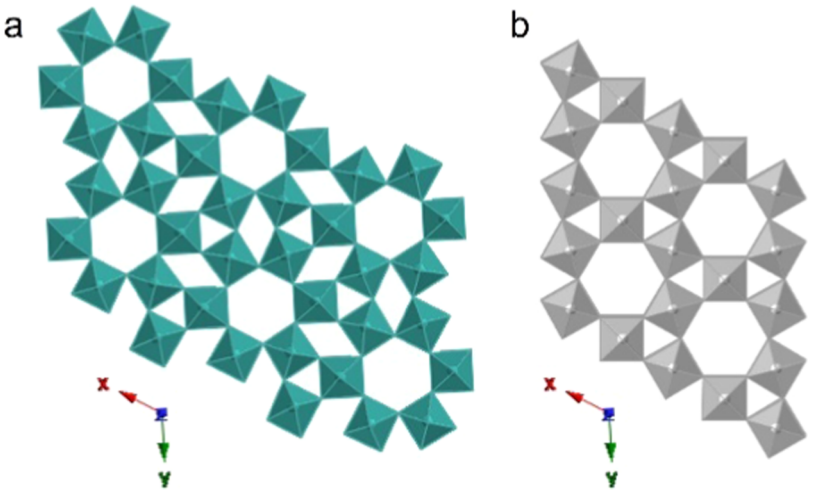

Figure 1. Schematic representation of crystallographic tunnel arrangement in (a) h'-WO_3 and (b) h-WO_3 polymorphs built from WO_6 octahedra (green and gray in (a) and (b), respectively).

of cations inside the structural channels can also modify the electronic properties of tungsten bronzes, as exemplified by the catalytic properties of tungsten bronzes for soot oxidation, which depends on the alkali cation modifying the electron donor behavior,[10] and by the plasmonic properties of bronzes with the h-WO_3 structure.[15]

Beyond the properties of bronzes, their conception also enables the design of further new materials. Indeed, cationic exchange enables the incorporation of additional transition metals in WO_3 frameworks. Exsolution of these metals by reductive treatment yields metal−tungsten oxide heterostructures with a controlled size of the exsoluted nanoparticles. This approach, applied to bronzes with the h-WO_3 structure, has enabled to tune CO_2 adsorption and then the selectivity of CO_2 reduction photocatalysis[13,16] through a strong metal−support interaction that triggered efficient charge transfer from h-WO_3 to the metallic nanoparticles. If such charge transfers are well documented for the usual WO_3 frameworks, they remain unexplored for the new h'-WO_3 structure, as well as the ability to exsolute metal nanoparticles from bronzes based on this structure.

In the present work, our objective is to question the ability of the h'-WO_3 framework to host foreign transition metal cations and to support charge transfer at its interfaces. To do so, we use the catalytic CO oxidation reaction as a probe of the charge density in platinum nanoparticles grown on h'-WO_3 nanostructures. Metal-h'-WO_3 heterostructures are designed by exsoluting the metal nanoparticles from cation-exchanged bronzes through the reduction of the inserted cations. We show that this approach can be generalized to several metals. By applying the exchange/exsolution process to the two different hexagonal tungsten bronze structures and by scrutinizing the kinetics of CO oxidation on the resulting heterostructures, we discuss in detail the role of the WO_3 structure on the charge density of the supported metal nanoparticles.

EXPERIMENTAL SECTION

h′*-$H_{0.07}WO_3$** and ***h*-WO_3** were prepared by hydrothermal synthesis, as described previously.[2] ***h′*-WO_3** doped with a metal M (*h′*-M_xWO_3) (M = Co, Cu, Pt, and Cs) was prepared by ionic exchange of the hexagonal hydrogen tungsten bronze (h′*-$H_{0.07}WO_3$**). 2 g of ***h′*-$H_{0.07}WO_3$** was suspended in a 15.1 × 10^{-3} M aqueous solution of a metal salt at room temperature. The metal-to-***h′*-$H_{0.07}WO_3$** ratio was selected to ensure a large excess of dopant in comparison with the hydrogen amount, i.e., 25 molar equivalents. The progress of the exchange reaction was followed by a pH decrease resulting from H^+ release from the hydrogen bronze material upon cationic exchange with the dopant. After stabilization of the pH for 30 min, the sample was washed by cycles of centrifugation−redispersion with Milli-Q water. Cobalt-, copper-, platinum-, and cesium-doped samples have been prepared by using $Co(NO_3)_2{\cdot}6\ H_2O$ (Sigma-Aldrich, 98%), $Cu(NO_3)_2{\cdot}2.5\ H_2O$ (Sigma-Aldrich, 98%), $Pt(NH_3)_4(NO_3)_4$ (Sigma-Aldrich, 99.995%), and $CsNO_3$ (Sigma-Aldrich, 99%). The samples prepared according to this procedure are denoted in this work as ***h′*-$CoWO_3$**, ***h′*-$CuWO_3$**, ***h′*-$PtWO_3$**, and ***h′*-$CsWO_3$**, respectively. For comparison, Pt deposition was also carried out on a classical ***h*-WO_3**[2] by the procedure described above for ***h′*-$PtWO_3$**, and a Pt(1.96 wt %)-SiO_2 sample, denoted as **Pt-SiO_2**, was also studied. It was synthesized by incipient impregnation of a SiO_2 carrier (Degussa Aerosil 380) with a 0.04 mol L^{-1} aqueous solution of Pt-$(NH_3)_4(NO_3)_2$ (99.995%, Sigma-Aldrich), using 2.5 mL of solution per gram of SiO_2.[17]

X-ray diffraction (XRD) patterns were recorded in a Bruker D8 Advance A25 Diffractometer with Bragg−Brentano configuration, equipped with a Cu source ($\lambda_{Cu-K\alpha1}$ = 1.54056 Å, $\lambda_{Cu-K\alpha2}$ = 1.54439 Å) and fixed slits, in the range 10−80° 2θ, using a 0.04° step size and 2 s of integration time.

X-ray fluorescence analysis was performed in a Panalytical Aχios spectrometer of wavelength dispersion with 4 kW excitation energy.

Samples for electron microscopy were deposited on carbon-coated copper grids by drop-casting butanol suspensions of nanoparticles. The transmission electron microscopy (TEM) study at low and high magnifications was performed with a JEOL 2100 transmission electron microscope operated at 200 kV. On such equipment, the resolution limit is about 0.25 nm. Particle size measurements were performed particle by particle on samples subjected to the CO oxidation reaction. The average metal particle diameters, d and d_v, were determined from the measurement of at least 70 metal particles. d and d_v were calculated using the following formula: $d = \Sigma n_i d_i / \Sigma n_i$ and $d_v = \Sigma n_i d_i^3 / \Sigma n_i d_i^2$, where n_i is the number of particles of diameter d_i.[18] Scanning transmission electron microscopy (STEM) was carried out with a JEOL JSM-ARM200F (Cold Emission Gun) microscope equipped with an aberration-corrected spherical probe operating at 80 kV. We did not observe any beam damage, as reported earlier.[2] High angle annular dark field (HAADF-STEM) images were acquired at 68−280 mrad inner and outer collection semiangles. In order to achieve chemical distribution information, Energy Electron-Loss Spectroscopy (EELS) was performed by using a GIF-Quantum ER spectrometer, implemented in a JEOL JSM-ARM200F, at 18 and 20.3

mrad inner and outer collection semiangles. EELS maps were acquired with 0.4 eV energy dispersion per channel and a 0.05 s acquisition time. EELS spectra were denoised through principal component analysis by using the multivariate statistical analysis (MSA) plugin from the Gatan DMS analysis toolbox.[19]

Unless specified otherwise, the flow rates and the volumes determined by H_2 chemisorption and H_2-TPR experiments are defined in normal conditions, i.e., at 273 K and 101 325 Pa.

Temperature-programmed reduction by hydrogen (H_2-TPR) experiments were performed by using Micromeritics 2920 equipment. About 50 mg of sample was introduced in the U-type reactor on a plug of quartz wool and purged by Ar (25 mL min^{-1}) for about 15 min. The samples were then submitted to H_2-TPR under 25 mL min^{-1} H_2 (5%)/Ar from RT to 900 °C (10 °C min^{-1}) and left at this temperature for about 10 min. The water release in H_2-TPR experiments was trapped with an isopropanol−liquid N_2 mixture prior to the TCD detector. A mass spectrometer (Pfeiffer Vacuum OmniStar) also allowed the qualitative monitoring of various M/Z ions at the outlet of the TCD detector in the course of the H_2-TPR experiments.

The platinum accessibility of **Pt-SiO$_2$** was evaluated via the irreversible chemisorption method using H_2 as the probe molecule. These measurements were performed in static mode at 25 °C using a conventional volumetric apparatus (Belsorp max, Bel Japan) on 0.1422 g of catalyst. Before H_2 chemisorption measurements, the sample was first reduced in H_2 (about 10 mL min^{-1}) at 300 °C for 2 h (3 °C min^{-1} heating rate), with subsequent evacuation at 400 °C for an additional 2 h. The **Pt-SiO$_2$** sample was then cooled under vacuum to 25 °C. Two H_2 isotherms were recorded at 25 °C with intermediate evacuation for 2 h at RT (Figure S1). The first H_2 isotherm leads to the total amount of adsorbed H_2, whereas the second isotherm leads to the amount of H_2 adsorbed reversibly. The amount of irreversible H_2 uptake (back-sorption method)[20] was estimated from a linearized Langmuir plot of the difference of both adsorption isotherms, from which the number of accessible Pt atoms was calculated assuming a stoichiometry of 1 hydrogen atom per surface Pt atom. In the case of **Pt-SiO$_2$**, the amount of irreversible H_2 uptake was estimated to be 0.49 mL g_{sample}^{-1}, which led to a Pt dispersion (D (%) defined as the number of Pt surface atoms/total number of Pt atoms × 100) of 43.8% and a mean spherical particle size of 2.6 nm. Due to the potential change in H/Pt stoichiometry, which was shown to be dependent on the basicity of the supporting oxides, the associated changes in Pt nanoparticles electron density,[21,22] and the potential dissolution of hydrogen as a ***h*′-H$_{0.07}$WO$_3$** bronze, H_2 was not used to probe the Pt accessibility of the WO_3-supported samples for which the size of the Pt nanoparticles was rather ascertained by TEM. An attempt to estimate Pt accessibility of ***h*′-PtWO$_3$** using CO as a probe chemisorption molecule also failed due to the very weak bonding of CO to Pt supported on the ***h*′-PtWO$_3$** material in agreement with the earlier work of Wang et al. over $PtWO_3$ samples.[23]

XP spectra were collected on an Omicron Scienta (Argus) X-ray photoelectron spectrometer using a monochromated Al Kα ($h\nu$ = 1486.6 eV) radiation source having a 280 W electron beam power. Charge compensation was carried out using an electron beam having an energy of 1 eV and an emission current of 5 μA. The emission of photoelectrons from the sample was analyzed at a takeoff angle of 45° under ultrahigh vacuum conditions (1 × 10^{-7} Pa). XP spectra of ***h*′-PtWO$_3$** and ***h*-PtWO$_3$** were collected at a pass energy of 20 eV for C 1s, O 1s, W 4f, and Pt 4f core XPS levels both in their fresh state and after in situ reduction by H_2(10%)/Ar at 300 °C (14 °C min^{-1}) for 20 min in the pretreatment chamber of the XPS facility. The O 1s signal at 530.5 eV (full width at half maximum, fwhm ∼1.5 eV) was used as a reference, rather than adventitious carbon,[24] to calibrate the binding energies (BEs) of C 1s, W 4f, and Pt 4f. All of the BEs reported in this work were measured with an accuracy of ±0.2 eV. The peak areas were determined after subtraction of a Tougaard background. The atomic ratio calculations were performed after normalization using Scofield factors.[25] Spectrum processing was carried out by using the Casa XPS software package and Origin 7.1 (Origin Lab Corporation).

CO oxidation experiments were carried out in a U-type quartz dynamic differential microreactor (10 mm internal diameter) with a total flow rate of 100 mL min^{-1}. The synthetic gas mixture was fed from independent cylinders (H_2, CO, O_2(50%)/He, and He from Air Liquide, 99.999% purity) via mass flow controllers (Brooks 5850TR and Bronkhorst F-201CV-200-RAD-11-V). The reactor outflow was analyzed using an μ-GC (Agilent, CP4900) equipped with two channels. The first channel used a 5A molecular sieve column (80 °C, 150 kPa He, 200 ms injection time, 37 s backflush time) and was used to quantify O_2 and CO. The second channel was equipped with a poraPlot Q column (100 °C, 150 kPa He, 50 ms injection time, 6 s backflush time) and was used to quantify CO_2. Prior to the reaction, the catalyst samples (30−50 mg diluted in either 400 mg of SiO_2 (Davisil, grade 62, 60−200 mesh) or 600 mg of α-Al_2O_3 (Sasol, CERALOX, 60−120 mesh) were reduced under 50 mL min^{-1} of H_2 at 300 °C for 0.5−1 h (3 °C/min heating rate). The catalyst temperature was then decreased to RT under H_2 before being flushed by 100 mL min^{-1} of He at RT. The CO(1%)−O_2(1%)−He was subsequently introduced, and temperature-programmed surface CO oxidation was performed under temperature transient (3 °C min^{-1}) and/or steady-state (steps of 10 to 5 °C) conditions up to 250−300 °C. The kinetic studies were performed at a steady state, while the reactor was operated isothermally and as close to a differential reactor as possible by limiting the CO conversion to <20%. The apparent activation energy of the CO oxidation reaction was determined from the catalytic data of the temperature-programmed CO oxidation in the 180−200 °C temperature range, whereas the reaction orders were determined at 190 and 200 °C on ***h*-PtWO$_3$** and ***h*′-PtWO$_3$** diluted in 600 mg of α-Al_2O_3 (CO reaction order determined with an O_2 concentration of 1.0% and CO concentrations varying from 1.0 to 1.94%, O_2 reaction order determined with a CO concentration of 1.0% and O_2 concentrations varying from 0.6 to 1.4%) and at 190 °C on **Pt-SiO$_2$** (32.8 mg), ***h*-PtWO$_3$** (40.7 mg), and ***h*′-PtWO$_3$** (39.9 mg) diluted in 400 mg of SiO_2 (CO reaction order determined with an O_2 concentration of 2.0% and CO concentrations varying from 1.0 to 2.2%, O_2 reaction order determined with a CO concentration of 1.0% and O_2 concentrations varying from 1.0 to 2.0%). CO conversions were calculated as follows: X_{CO} (%) = $[CO_2]/[CO]_i \times 100$, where $[CO_2]$ and $[CO]_i$ were the CO_2 concentration measured at the outlet of the reactor and the initial CO concentration, respectively. C and O mass balances were found to be 100 ± 2%.

The number of surface-accessible Pt sites Pt_s (mol g^{-1}) was estimated according to the following equation:

$$Pt_s = sw\frac{\text{Pt wt \%}}{M_{Pt}D}$$

where sw is the weight of the sample introduced in the reactor (g), Pt wt % is the Pt content, M_{Pt} is the Pt atomic weight, and D is the Pt dispersion (%) estimated either by H_2 chemisorption measurements (**Pt-SiO$_2$**) or by TEM (***h*′-PtWO$_3$** and ***h*-PtWO$_3$**), where $D = 6(v_m/a_m)/d_v$ (v_m (15.10 Å^3), a_m (8.07 Å^2), and d (Å) are the volume occupied by a Pt bulk atom, the area occupied by a surface Pt atom, and the volume-weighted mean diameter of the Pt particles, respectively.[18]

The turnover frequency (TOF, s^{-1}),[26] defined as the rate of reaction per Pt surface atom, was calculated according to the following equation

$$TOF = (F_{CO} \times X_{CO}/\nu \times sw)/Pt_s$$

where F_{CO}, X_{CO} and ν are the CO molar flow rate (mol s^{-1}), the CO conversion (%), and the stoichiometric coefficient of the reaction (2, from the reaction $2CO + O_2 = 2CO_2$), respectively.

RESULTS AND DISCUSSION

Structural and Compositional Characterization of the Materials. The final products of the cationic exchange reactions between ***h*′-H$_{0.07}$WO$_3$** nanoplatelets and the metal

dopants in aqueous suspensions were characterized through several diffractometric and spectroscopic techniques. XRD confirms that the bronze structure (S.G. *P6/mmm*) is maintained after exchange of the protons (Figure S2, Table S1). Additionally, a crystalline impurity (2θ = 49.3°), already detected in the ***h′*-$H_{0.07}WO_3$** precursor, is also present in the cation-exchanged materials (Figure S3), presumably ascribed to tungsten oxide.[2] The increase of the *a* cell parameter (Table S1) in the exchanged materials suggests a slight structural modification, with an enlargement of the cell in the plane perpendicular to the tunnels (Figure 1). This feature might be related to the substitution of H^+ by a greater size cation inside the tunnels and/or due to a partial reduction of W^{6+} (0.60 Å) to W^{5+} (0.62 Å).[27] This supports the incorporation of foreign cations inside the tunnels by at least partial H^+ exchange.

The cationic compositions measured by X-ray fluorescence (XRF, Table 1) suggest successful incorporation of the dopants

Table 1. Chemical Composition of Doped *h′*-WO_3 Samples Estimated by XRF

	chemical composition (weight %)			
material	dopant	W	O	estimated composition
***h′*-$CoWO_3$**	1.21	78.34	20.44	$Co_{0.05}WO_3$
***h′*-$CuWO_3$**	0.44	85.37	14.18	$Cu_{0.03}WO_3$
***h′*-$PtWO_3$**	2.44	77.37	20.19	$Pt_{0.03}WO_3$
***h′*-$CsWO_3$**	3.83	76.27	19.90	$Cs_{0.07}WO_3$
***h*-$PtWO_3$**	2.93	76.98	22.60	$Pt_{0.04}WO_3$

by H^+ exchange with monovalent (Cs^+) or divalent (Cu^{2+} and Pt^{2+}) cations. The amount of Co species exceeds the maximal exchange rate of H^+ by accounting for Co^{2+} cations. This might originate from further reduction of W^{6+} to W^{5+} in the exchanged bronze.

Low magnification TEM images (Figures 2a,c,e,g and S2b) show nanoplatelets with morphology and size similar to those observed for the pristine bronze. The crystal structure is also confirmed by HRTEM and the corresponding FFTs (insets in Figure 2b,d,f,h). For all samples, including the Co-doped one, we did not observe any morphology other than the typical bronze platelets.

XRD (Figure S2) and TEM (Figure 2) do not suggest the formation of additional crystalline phases or modification of the particle morphologies, as expected from ionic exchange reactions. The protons in the initial *h′*-WO_3 framework are located in the $(WO_6)_6$ hexagonal channels oriented along the *c* direction.[2] Therefore, we can reasonably assume that cationic exchange leads to metal cations located in these channels. This hypothesis is confirmed by scanning transmission electron microscopy (STEM) imaging studies of the Pt- and Cs-doped samples. In both materials, atomically resolved STEM coupled to high angle annular dark field (HAADF) and to annular bright field (ABF) detections (Figures 3 and S4) show the six and 4-fold channels characteristic of the *h′* bronze, as marked in Figures 3a and S4a. Additionally, STEM-HAADF shows a relatively high disorder degree in these materials due to antiphase boundaries (APB, yellow dashed lines in Figures 3a and S4a), as previously described in pristine ***h′*-$H_{0.07}WO_3$**,[2] giving rise to the formation of the *c*-WO_3[28] characteristic octahedral arrangement not only perpendicular to this defect (Figures 3a and S4g) but also extended to wider regions (Figure S4a,e). Furthermore, the significant presence of defects in these materials is also reflected by XRD since crystalline domains are smaller than 10 nm (Table S1) while the nanoplatelet size is around 40−60 nm (Figure 2).

It should also be noticed that additional contrasts in the center of the hexagonal channels (yellow arrows in Figures 3 and S4b) are locally observed, suggesting the presence of Cs and Pt, for the respectively doped samples. EELS analysis (Figure 4) confirms the presence of Cs according to the sum spectra acquired in two energy windows, which show the characteristic O-K, Cs-$M_{4,5}$, and W-$M_{4,5}$ edges. Such an analysis is not possible in the Pt-doped sample because of the overlapping of W-$M_{4,5}$ (1809 eV) and Pt-$M_{4,5}$ (2122 eV) edges (Figure S5).

For comparison, we have also addressed cationic exchange within the ***h*-WO_3** framework by focusing on Pt doping. XRD and TEM images (Figure S6 and Table S2) confirm that the *h*-WO_3[29] bronze structure (S.P. *P6/mmm*) is maintained after Pt cationic exchange. The Pt/W atomic ratio estimated by XRF is 0.04 (Table 1). However, high-magnification TEM images (Figure S6e) show the formation of 1.7 ± 0.4 nm Pt nanoparticles (d_v, volume-weighted particle size, Table S3) over the *h*-WO_3 surface, contrary to the ***h′*-WO_3**-based materials for which Pt particles could not be observed, thus suggesting that the dopants are incorporated inside the structural channels of the *h′* form.

***In Situ* Formation of Platinum Nanoparticles from Exchanged Hexagonal Tungsten Oxide Bronzes.** The H_2 temperature-programmed-reduction (H_2-TPR) of the ***h′*-$H_{0.07}WO_3$** material (Figure 5a) shows a complex reduction profile, with reduction onset at about 500 °C with a maximum at 710 °C, followed by a reduction tail at temperatures higher than 800 °C. The H_2 profile recorded by mass spectrometry (MS) (Figure S7b) is fully consistent with the thermal conductivity detector (TCD) signal (Figures 5a and S7a). The reduction profile of ***h′*-WO_3** (Figure 5a) is in rather good agreement with that reported earlier by Depuccio et al. on a more traditional WO_3 support for which the reduction peaks below 550 °C were assigned to the surface reduction of WO_3 to substoichiometric $WO_{2.9}$, whereas those from 700 to 900 °C were assigned to the reduction of $WO_{2.9}$ to WO_2.[30]

The H_2-TPR profile recorded on a fresh ***h′*-$PtWO_3$** sample shows 5 contributions at 100, 175, 210, 450, and 645 °C, among which that at 175 °C is the only negative one (Figure 5b, green trace). As was the case for H_2-TPR performed on ***h′*-WO_3** (Figures 5a and S7), the TCD-recorded contributions for ***h′*-$PtWO_3$** correlate with those recorded for the H_2 trace by MS (Figure S8). NO and N_2O contributions of very low intensity were also recorded in the course of the latter H_2-TPR experiment (Figure S8b). The formation of such species is likely attributed to the reduction of the nitrate counteranions of the Pt^{2+} precursor ($Pt(NH_3)_6(NO_3)_2$). The release of NO_x species does not seem to influence the TCD signal to a significant extent, as the latter (Figure S8a) is consistent with the H_2 MS trace (Figure S8b). Reduction of Pt ions in the *h′*-WO_3 framework occurs at a much lower temperature, i.e., 100 °C (Figure 5b, green trace), than that reported earlier by Wang et al. (~180 °C),[23] which can be explained by the different nature of the WO_3 materials and Pt precursors. Besides, a negative peak is observed in the present work, which is attributed to the release of H_2, whose exact origin, i.e., Pt and/or WO_3 phases, cannot be ascertained from the experiments carried out up to now. The fact that this negative contribution is observed at the temperature (~ 180 °C) for which Pt ion

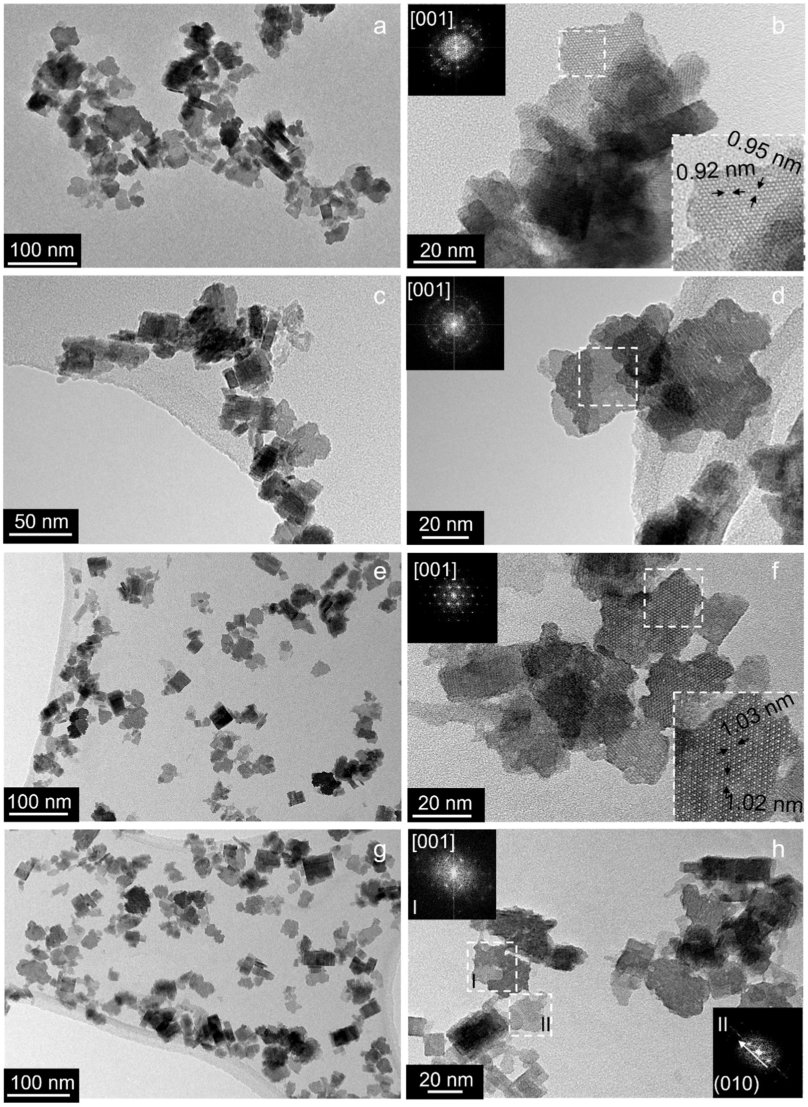

Figure 2. (a, c, e, g) Low and (b, d, f, h) high-magnification TEM images of (a, b) Co, (c, d) Cu, (e, f) Pt, and (g, h) Cs-doped materials. Insets in (b), (d), (f), and (h) correspond to the Fast Fourier Transforms (FFTs) and to enlarged regions of the areas delimited by white dashed squares.

reduction was observed by Wang et al.[23] may explain why this negative contribution could not be observed previously.[23] The H_2 consumption at about 645 °C and the tail at temperatures higher than 700 °C on the ***h′*-PtWO$_3$** sample (Figure 5b, green trace) can be attributed to the reduction of ***h′*-WO$_3$** from the support and is shifted to lower temperatures compared to the pristine ***h′*-WO$_3$** material, which is likely due to the presence of Pt.[31]

The maximum intensity of the low-temperature Pt^{2+} reduction peak is similar on both the ***h*-PtWO$_3$** and ***h′*-PtWO$_3$** samples (Figure 5b, red and green traces, respectively). The H_2 consumption in this low-temperature reduction peak was roughly estimated to be 13.8 and 8.7 mL of H_2 g^{-1} for ***h*-PtWO$_3$** and ***h′*-PtWO$_3$**, respectively. On the basis of Pt contents of 2.93 and 2.44 wt % (Table S3) for ***h*-PtWO$_3$** and ***h′*-PtWO$_3$**, the corresponding H_2/Pt ratios were estimated to be 4.1 and 3.1, respectively. The fact that both ratios well exceed the theoretical H_2/Pt ratio of 1 for the reduction of Pt^{2+} indicates an additional reduction of surface W species in contact with Pt species and/or additional reduction of the nitrate counterions of the Pt precursor. The higher H_2/Pt ratio evaluated for ***h*-PtWO$_3$** may also be due to the more difficult integration of the corresponding peak, which is broader than that for ***h′*-PtWO$_3$**.

Overall, the H_2-TPR experiments performed on ***h′*-PtWO$_3$** and ***h*-PtWO$_3$** indicate that the Pt^{2+} ions should be fully reduced below 300 °C on both WO_3 supports and that the Pt^{2+} species supported on *h′*-WO_3 should be in lower interaction with this support compared to those supported on *h*-WO_3, as indicated by the lower reduction temperature of the Pt^{2+} ions on ***h′*-PtWO$_3$** (100 °C) compared to ***h*-PtWO$_3$** (157 °C) in Figure 5b.

Electronic States of Platinum-Based Materials. The WO_3-supported Pt samples were characterized by XPS both in their fresh state and after *in situ* reduction by H_2(10%)/Ar at 300 °C (14 °C min^{-1}) for 20 min in the pretreatment chamber of the XPS facility. The corresponding O 1s, W 4f, and Pt 4f XP spectra of ***h′*-PtWO$_3$** and ***h*-PtWO$_3$** are shown in Figure 6, with the associated data listed in Table 2. In their fresh state, both samples show a W $4f_{7/2}$ signal with a binding energy (BE) of about 35.7 eV, which is consistent with the presence of W^{6+} in both WO_3 materials.[32] After *in situ* reduction, the width of the W 4f peaks increases and a contribution appears at lower BE (BE ~ 32 eV), which indicates the reduction of W^{6+}, as

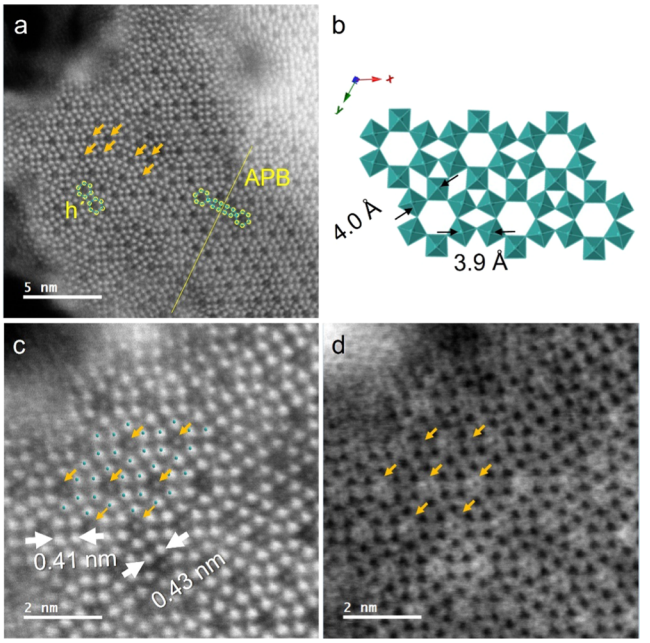

Figure 3. STEM study of ***h′*-CsWO$_3$**: (a) Atomically resolved HAADF image, (b) scheme of the *h′*-WO$_3$ crystal structure of the bronze, oriented along the (001) direction and superimposed to the image (c) (green dots account for W atom columns). (c) High-magnification STEM-HAADF and (d) corresponding STEM-ABF images simultaneously acquired. Orange arrows in (a), (c), and (d) indicate contrast not observed in pristine ***h′*-H$_{0.07}$WO$_3$**.[2] Antiphase boundary defects are outlined in comparison with regions without defects (*h′*) in (a).

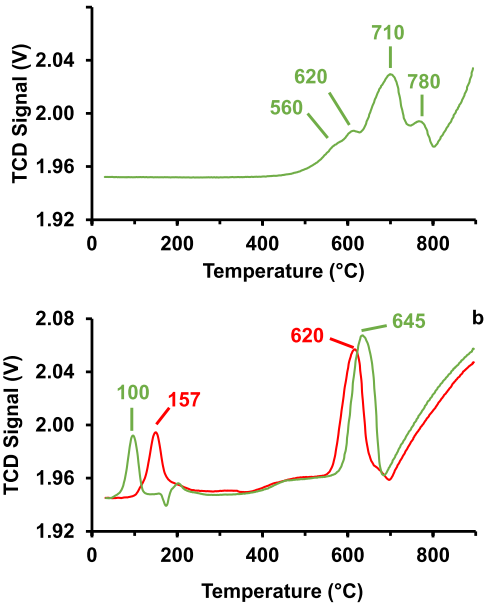

Figure 5. Thermal conductivity detector traces recorded in the course of the H$_2$-TPR experiments carried out on (a) ***h′*-H$_{0.07}$WO$_3$**, (b) ***h′*-PtWO$_3$** (green), and ***h*-PtWO$_3$** (red) at 10 °C min^{-1} under 25 mL min^{-1} H$_2$(5%)/Ar. The sample preparations are detailed in the Experimental section.

further supported by the significant decrease in the O/W at. ratio (Table 3). The BE of the Pt 4f$_{7/2}$ signal varies from 73.4 to 72.8 eV in the fresh ***h′*-PtWO$_3$** and ***h*-PtWO$_3$** samples, respectively, in agreement with the presence of Pt^{2+} ions. After reduction, the BE Pt 4f$_{7/2}$ signal shifts down to 71.4 and 71.2 eV for ***h′*-PtWO$_3$** and ***h*-PtWO$_3$**, respectively, which confirms the reduction of Pt^{2+} to Pt^0. As expected for well-dispersed metal nanoparticles supported on an oxide,[33] the surface Pt/W ratios determined by XPS remained higher than or equal to the bulk ones estimated by XRF (Table 2), as the proportion of Pt atoms analyzed by XPS in small particles should be higher than that of the W atoms buried in the core of thicker WO$_3$ particles. The decrease in the Pt/W at. ratio (Table 1) is higher over *h′*-WO$_3$ than over *h*-WO$_3$, which indicates more pronounced sintering of Pt particles in ***h′*-PtWO$_3$** than in ***h*-PtWO$_3$**, in agreement with H$_2$-TPR showing weaker interaction of Pt^{2+} ions with *h′*-WO$_3$ (Figure 5b). By applying a model proposed by Kerkhof and Moulijn,[34] we evaluate from XPS the Pt particle sizes to 1.7 and 0.4 nm (Table 2) in *in situ* reduced ***h′*-PtWO$_3$** and ***h*-PtWO$_3$**, respectively (by using surface areas 55 and 45 m^2 g^{-1},[2] and 2.44 and 2.93 wt % Pt

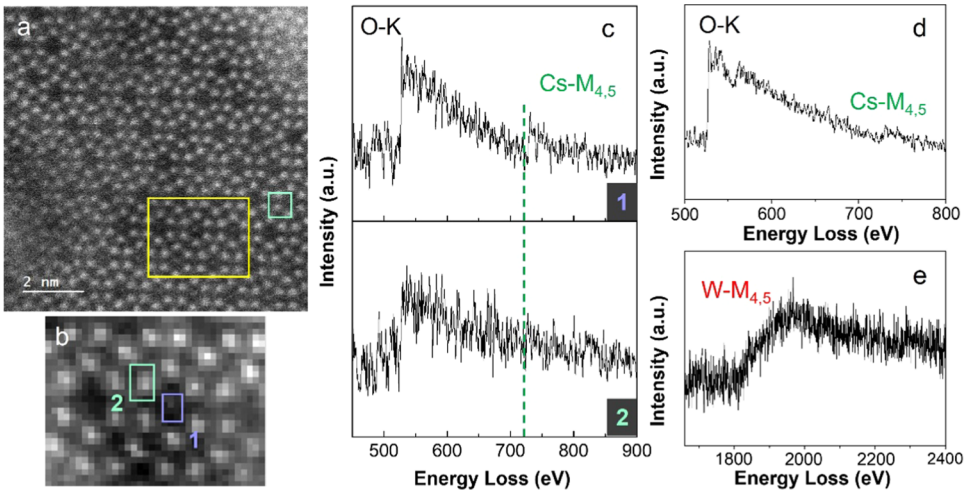

Figure 4. EELS-STEM study of ***h′*-CsWO$_3$**: (a) STEM-HAADF image of a nanoparticle oriented along the [001] zone axis, (b) STEM-HAADF image simultaneously acquired with EELS spectra. (c) Top and down spectra correspond to the Cs-M$_{4,5}$ edge in purple and green regions in (b), respectively. (d) Sum spectra of the yellow area in (a) corresponding to the 500−800 eV energy window showing the O−K and Cs-M$_{4,5}$ edges. (e) Sum spectra of the yellow area in (a) corresponding to the 1600−2400 eV energy window showing the W-M$_{4,5}$ edge.

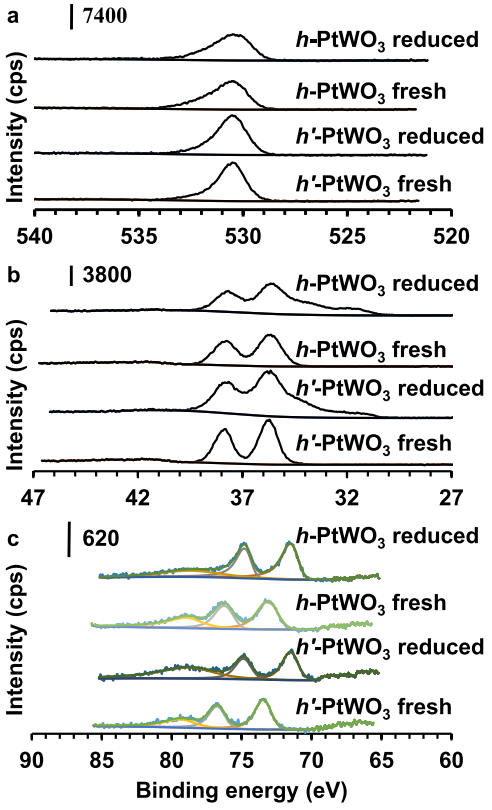

Figure 6. (a) O 1s, (b) W 4f, and (c) Pt 4f XP spectra of ***h*-PtWO$_3$** and ***h'*-PtWO$_3$** in their fresh and *in situ* reduced states. The binding energies were referenced to the O 1s binding energy at 530.5 eV.

Table 2. XPS Data for *h'*-PtWO$_3$ and *h*-PtWO$_3$

	BE (eV)		atomic ratio surface		atomic ratio bulk	
samples	W 4f$_{7/2}$	Pt 4f$_{7/2}$	O/W	Pt/W	Pt/W	Pt size (nm)[a]
***h'*-PtWO$_3$ fresh**	35.7	73.4	3.9	0.0567		
***h'*-PtWO$_3$ reduced**	35.7	71.4	2.4	0.0291	0.0298	1.7
***h*-PtWO$_3$ fresh**	35.6	72.8	4.1	0.0756		
***h*-PtWO$_3$ reduced**	35.7	71.2	2.9	0.0613	0.0358	0.4

[a]Estimation based on the model of Kerkhof and Moulijn by considering spherical Pt particles.[34]

contents for ***h'*-PtWO$_3$** and ***h*-PtWO$_3$**, respectively). Finally, according to the decrease in the O/W ratio (Table 2), *h'*-WO$_3$ is more reduced than *h*-WO$_3$ in the reduced Pt-containing samples, in agreement with the greater intensity of the high-temperature reduction peak at about 620−645 °C observed for ***h'*-PtWO$_3$** compared to that observed for ***h*-PtWO$_3$** (Figure 5b).

CO Oxidation Kinetics. *CO Oxidation on h'-PtWO$_3$ and h-PtWO$_3$.* Steady-state catalytic CO oxidation from 160 to 240 °C and associated activation energies measured on ***h'*-PtWO$_3$** (75 kJ mol^{-1}) and ***h*-PtWO$_3$** (86 kJ mol^{-1}) diluted in SiO$_2$ are shown in Figures 7a,b and 8a,b, respectively. The same experiments have been performed on the **Pt-SiO$_2$** sample for comparison (see detailed discussion in the SI associated with Figure S9). Activation energies are similar on the PtWO$_3$ samples and on **Pt-SiO$_2$** (Figure S9b, blue traces). In contrast, the reaction orders with respect to CO and O$_2$ measured at 190 °C on ***h'*-PtWO$_3$** (Figure 7c,d) and ***h*-PtWO$_3$** (Figure 8c,d) are substantially different from those determined on **Pt-SiO$_2$** (Figure S9c,d, Table 3). The reaction orders on the PtWO$_3$ samples were found to be reproducible under slightly different operating conditions (Table 3). The shift of the CO reaction order to more negative values with increasing temperature on ***h*-PtWO$_3$** (Table 3) is consistent with earlier findings of Cant et al.[35]

The stronger interaction between Pt species and the *h*-WO$_3$ polymorph is further confirmed by TEM images of samples after CO oxidation reaction (Figure 9a,b,d), which show Pt nanoparticles with narrower particle size distribution for ***h*-PtWO$_3$** than ***h'*-PtWO$_3$**, as well as lower volume-weighted platinum particle size for ***h*-PtWO$_3$** (Table 4).

Comparison of CO Oxidation Catalytic Activities and Kinetic Data Measured under Steady State. Figure 10 shows that ***h*-PtWO$_3$** (red trace) performs slightly better in the catalytic CO oxidation reaction compared to ***h'*-PtWO$_3$** (green trace) and **Pt-SiO$_2$** (blue trace). The activation energy is similar for all catalysts (about 80 kJ mol^{-1}, Table 3). The most active catalyst, namely, ***h*-PtWO$_3$**, also shows the most negative reaction order with respect to CO, followed by **Pt-SiO$_2$** and ***h'*-PtWO$_3$** (Table 3). ***h*-PtWO$_3$** also exhibits the most positive reaction order with respect to O$_2$, whereas the O$_2$ reaction order decreases for **Pt-SiO$_2$** and then ***h'*-PtWO$_3$** (Table 3). The quasi-first-order dependence with respect to O$_2$ for ***h*-PtWO$_3$** is consistent with an increased coverage of the Pt nanoparticles by CO (more negative CO reaction order) and a greater difficulty for O$_2$ to adsorb on a free Pt site. It indicates that the rate-determining step of the catalytic CO oxidation reaction should be the molecular adsorption of O$_2$.[36] This step should no longer be rate-determining for the other samples according to the decrease in the O$_2$ reaction order, likely due to a lower CO coverage (less negative CO reaction orders).

Table 3. Kinetic Data of the CO Oxidation Reaction on the Supported Pt Catalysts[a]

sample	sw[b] (mg)	diluent weight (g)	*T* (°C)	gas feed[c]	E_a[d] (kJ mol^{-1})	CO reaction order (α)	O$_2$ reaction order (β)
***h*-PtWO$_3$**	40.7	0.4 SiO$_2$	190	l	86.2^{ss}, 90^{t}	−0.64	0.97
	40.0	0.6 Al$_2$O$_3$	190	l-r	68^{t}	−0.55	0.91
	50.8	0.6 Al$_2$O$_3$	200	l-r	81^{t}	−0.70	1.16
Pt-SiO$_2$	32.8	0.4 SiO$_2$	190	l	86.0^{ss}	−0.37	0.84
***h'*-PtWO$_3$**	39.9	0.4 SiO$_2$	190	l	75.4^{ss}	−0.19	0.62
	40.0	0.6 Al$_2$O$_3$	190	l-r	65^{t}	−0.08	0.59

[a]CO and O$_2$ reaction orders were determined at 190 or 200 °C in order to maintain the CO conversion below 10%, whereas activation energies were determined under either transientt or steady-state^{ss} conditions. [b]Sample weight. [c]Lean mixtures (l), lean-rich mixtures (l-r). [d]Apparent activation energy.

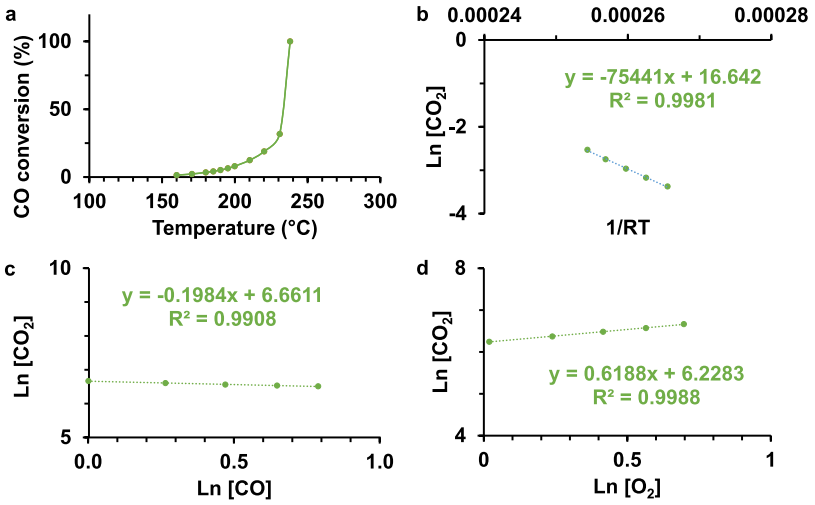

Figure 7. Catalytic oxidation of CO by O_2 on ***h′*-PtWO$_3$** diluted in SiO_2 with a total flow rate of 100 mL^{-1} min: (a) steady-state CO(1.0%)-O_2(1.0%)-He reaction, (b) apparent activation energy (E_a) determined from about 180 to 200 °C from the data in (a), (c) CO reaction order determined at 190 °C with an O_2 concentration of 2.0% and CO concentrations varying from 1.0 to 2.2% and (d) O_2 reaction order determined at 190 °C with a CO concentration of 1.0% and O_2 concentrations varying from about 1.0 to 2.0%. The reaction orders were estimated in lean mixtures (excess of oxygen compared to stoichiometry).

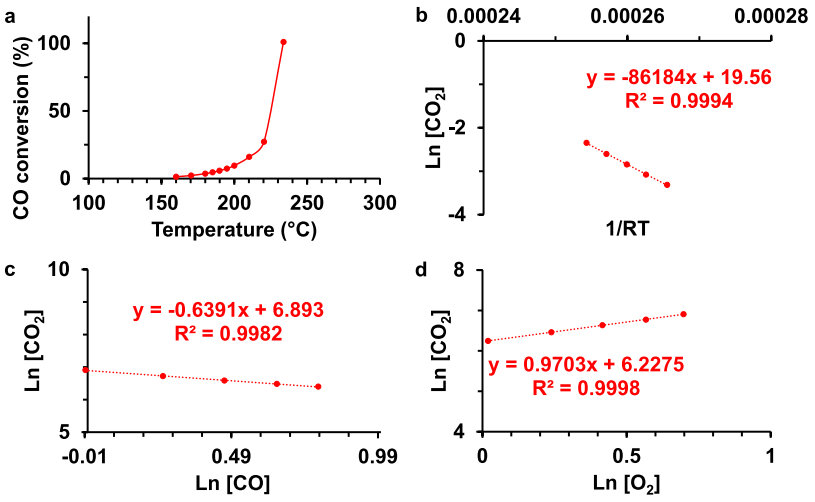

Figure 8. Catalytic oxidation of CO by O_2 on ***h*-PtWO$_3$** diluted in SiO_2 with a total flow rate of 100 mL min^{-1}: (a) steady-state CO(1.0%)-O_2(1.0%)-He reaction, (b) apparent activation energy (E_a) determined from about 180 to 200 °C from the data reported in (a), (c) CO reaction order determined at 190 °C with an O_2 concentration of 2.0% and CO concentrations varying from 1.0 to 2.2% and (d) O_2 reaction order determined at 190 °C with a CO concentration of 1.0% and O_2 concentrations varying from about 1.0 to 2.0%. The reaction orders were estimated in lean mixtures (excess of oxygen compared to stoichiometry).

Therefore, the catalytic CO oxidation performance of the various samples shown in Figure 10 is not exclusively related to the intrinsic kinetic parameters E_a, the apparent activation energy, and α and β, the reaction orders with respect to CO and O_2, respectively, it also depends to a significant extent on the number of surface-accessible Pt sites (Pt_s). The Pt atomic weight (sw), Pt dispersion (D), the volume-weighted mean diameter of the Pt particles (d), and Pt_s values are shown in Table 5. Pt_s values indicate a correlation with the CO oxidation catalytic performance at low CO conversion (Figure 10): the higher Pt_s, the higher the conversion from **Pt-SiO$_2$** to ***h′*-PtWO$_3$** and then ***h*-PtWO$_3$**.

We have then estimated the turnover frequency (TOF, s^{-1}),[26] defined as the rate of reaction per Pt surface atom, in order to enable a more reliable comparison of the catalytic activities. First, the TOF measured on **Pt-SiO$_2$** at 180 °C (0.008 s^{-1}) is in good agreement with that reported earlier by Cant et al. on a similar sample (0.04 s^{-1})[35] at a comparable temperature (Table 6). The TOF measured at 200 °C on **Pt-SiO$_2$** (0.02 s^{-1}) is also lower than that reported by Bera et al. over a Pt−Al_2O_3 catalyst (0.13 s^{-1}),[37] although the origin of the reported TOF is unclear (see details in the SI). At 180 °C, the TOFs we measured show that ***h′*-PtWO$_3$** and ***h*-PtWO$_3$** are slightly less active than the **Pt-SiO$_2$** catalyst, contrary to the CO conversion data (Figure 10). ***h′*-PtWO$_3$** is slightly more active than ***h*-PtWO$_3$**. Extrapolation[17] (Table 6) of the TOFs at 120 °C of ***h′*-PtWO$_3$** and ***h*-PtWO$_3$** measured at 180 °C, considering the activation energies determined under steady-state conditions (Table 3), would indicate that the presently studied ***h′*-PtWO$_3$** and ***h*-PtWO$_3$** catalysts are much less active than those reported earlier by Wang et al.[23] (Table 6). Therefore, the rather good agreement between the TOF of **Pt-**

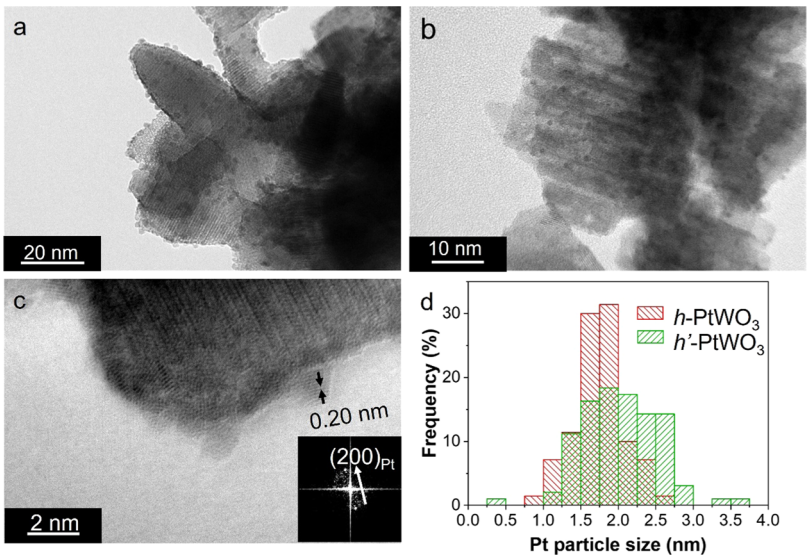

Figure 9. Low magnification TEM images of reduced (a) ***h′*-PtWO$_3$** and (b) ***h*-PtWO$_3$** samples. (c) High-magnification TEM image of reduced ***h′*-PtWO$_3$**. (d) Corresponding size distributions of the Pt nanoparticles supported on the reduced ***h′*-PtWO$_3$** and ***h*-PtWO$_3$** samples, respectively.

Table 4. Average Metal Particle Diameters, *d* and d_v, of the Supported Platinum Nanoparticles after Catalytic Oxidation by O_2

	d (nm)	d_v (nm)
reduced ***h′*-PtWO$_3$** (*h′*-$Pt_{0.03}WO_3$)	2.0 ± 0.5	2.3 ± 0.6
reduced **h-PtWO$_3$** (h-$Pt_{0.04}WO_3$)	1.7 ± 0.3	1.9 ± 0.4

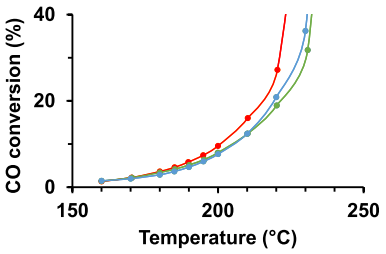

Figure 10. CO conversion in the CO−O_2 catalytic reaction as a function of reaction temperature on ***h*-PtWO$_3$** (red trace), ***h′*-PtWO$_3$** (green trace), and **Pt-SiO$_2$** (blue trace) diluted in SiO_2, with a 100 mL min^{-1} total flow rate of CO(1.0%)−O_2(1.0%)−He.

SiO$_2$ with that of Cant et al.[35] at 180 °C would no longer be valid at 120 °C. This indicates that such an extrapolation may be hazardous, in particular, as the activation energy and the reaction order of the CO oxidation reaction vary with the reaction temperature.[35] This prevents a fair comparison of the CO oxidation catalytic performances of the **Pt-WO$_3$** catalysts with that of reported Pt-WO_3 catalysts.[23] We could not measure the catalytic performances of ***h′*-PtWO$_3$** and ***h*-**

Table 6. Comparison of the CO Oxidation Turnover Frequencies of the Supported Pt Samples with Those of Earlier Studies

catalysts	O_2/CO ratio	temperature (°C)	TOF (s^{-1})	refs
Pt-SiO$_2$	0.64/1.28	127	0.008	35
Pt-SiO$_2$	1.00/1.00	120	0.00023[a]	This work
***h′*-PtWO$_3$**	1.00/1.00	120	0.00025[a]	
***h*-PtWO$_3$**	1.00/1.00	120	0.00011[a]	
Pt/C-WO$_3$	20.0/1.00	120	0.0083	23
Pt/DBD-WO$_3$	20.0/1.00	120	0.0166	
Pt-SiO$_2$	0.64/1.28	177	0.04	35
Pt-SiO$_2$	1.00/1.00	180	0.0075	this work
***h′*-PtWO$_3$**	1.00/1.00	180	0.0052	
***h*-PtWO$_3$**	1.00/1.00	180	0.0037	
Pt/Al_2O_3		200	0.13 (1.58)[b]	37
Pt-SiO$_2$	1.00/1.00	200	0.0200	this work
***h′*-PtWO$_3$**	1.00/1.00	200	0.0122	
***h*-PtWO$_3$**	1.00/1.00	200	0.0099	

[a]TOF extrapolated at 120 °C from the reaction rate measured at 180 °C and activation energies determined under steady-state conditions listed in Table 3. [b]TOF value estimated from a reaction rate of 12.92 μmol/g s listed by Bera et al.[37] and a Pt dispersion of 16% (Pt particles of 7 nm) in their work. It was not possible to extract the exact gas composition in terms of CO and O_2 concentrations under which the measurements were performed, which may affect the reaction rate to a significant extent.

Table 5. Amount of Pt Surface-Accessible Atoms (Pt_s), Pt Weight Content (Pt), Dispersion (*D*), and Mean Diameter of Pt Nanoparticles (*d*) in the Samples Leading to the CO Oxidation Performance Shown in Figure 10

sample	sw[a] (g)	Pt (wt %)	*D*[b] (%)	*d*[f] (nm)	Pt_s[g] (μmol/aliquot of sample)	Pt_s[g] (μmol/g_{sample})
***h*-PtWO$_3$**	0.0407	2.93	59.1[c]	1.9	3.61	88.8
***h′*-PtWO$_3$**	0.0399	2.44	48.8[c]	2.3	2.43	61.0
Pt-SiO$_2$	0.0328	1.96	43.8[d,e]	2.6	1.44	44.0

[a]Sample weight. [b]Pt dispersion estimated either by TEM (***h′*-PtWO$_3$** and ***h*-PtWO$_3$**) [c]or chemisorption (**Pt-SiO$_2$**) [d,e]mean diameter of the Pt particles, amount of Pt surface accessible sites [f]in the aliquot of sample and. [g]per gram of sample.

PtWO$_3$ under Wang et al.'s experimental conditions, as the authors did not explicitly report the sample weight to flow rate ratio.[23]

Under similar experimental conditions, the slightly superior CO oxidation performance of ***h′*-PtWO$_3$** compared to ***h*-PtWO$_3$** (Table 6) can be attributed to a higher global reaction order (Table 3) for ***h′*-PtWO$_3$** ($\alpha + \beta \sim 0.47$) compared to ***h*-PtWO$_3$** ($\alpha + \beta \sim 0.34$). The significantly higher CO reaction order for ***h′*-PtWO$_3$** (-0.14 ± 0.05) compared to ***h*-PtWO$_3$** (-0.60 ± 0.04) may be attributed to a higher electron density of the Pt nanoparticles supported on partially reduced h'-WO$_3$ than on partially reduced h-WO$_3$, due to a higher electron transfer from ***h′*-WO$_3$** than from ***h*-WO$_3$**. The electron-richer Pt nanoparticles would bind less strongly to CO,[17] resulting in a lower CO coverage and a lower inhibition effect of CO on the CO oxidation catalytic reaction (less negative CO reaction order) for ***h′*-PtWO$_3$**. This interpretation would also account for the decrease of the O_2 reaction order from quasi-first order on ***h*-PtWO$_3$** (0.94 ± 0.03, Table 3) to quasi-half reaction order on ***h′*-PtWO$_3$** (0.61 ± 0.01, Table 3), which would agree with the potential change in the rate-determining step of the CO oxidation reaction from associative O_2 molecular adsorption on ***h*-PtWO$_3$** to dissociative O_2 adsorption on ***h′*-PtWO$_3$**, due to a lowering of the CO coverage of the Pt nanoparticles on partially reduced ***h′*-WO$_3$**. The higher electron transfer to Pt nanoparticles from partially reduced ***h′*-WO$_3$** than from partially reduced ***h*-WO$_3$** is further supported by the superior reducibility of the ***h′*** framework indicated by H_2-TPR (Figure 5b) and XPS (O/W ratio in Table 2). In contrast to a previous study by Thomas and co-workers,[17] such an electron enrichment of Pt nanoparticles could not be ascertained by XPS as the change in Pt $4f_{7/2}$ BE between the two samples (0.2 eV) remained within the accuracy of the XPS technique (±0.2 eV). This is not surprising as a 3-fold increase in CO oxidation TOF at 280 °C of electron-enriched Pt surface atoms was reported earlier, together with a decrease in the Pt $4f_{7/2}$ BE of 1.1 eV,[17] while we measured only a TOF increase of about 40% from ***h*-PtWO$_3$** to ***h′*-WO$_3$** at 180 °C (Table 6). This slight difference in electron transfer may be related to the close crystal structures and electronic structures of ***h*-WO$_3$** and ***h′*-WO$_3$**.[2]

We note that previous investigations addressing charge transfer at the WO$_3$–metal interface, as reported by Wang et al. for catalytic CO oxidation on m-WO$_3$–Pt heterostructures,[23] have relied on XPS and on DRIFT to probe the Pt $4f_{7/2}$ binding energy and a CO-Pt band, respectively. However, the observed downshift of the Pt $4f_{7/2}$ binding energy of 0.2 eV is within the accuracy of the XPS technique, and the analysis of a 5 cm^{-1} shift of a CO-Pt band at 2085 cm^{-1} can be made complex by the contributions of gaseous CO. Herein, we show that the kinetics of CO oxidation catalysis themselves are efficient probes to address charge transfer at the interfaces of WO$_3$ materials.

CONCLUSIONS

Cation exchange has been shown as a straightforward path to design nanoplatelets of doped hexagonal tungsten bronzes. Especially we could incorporate Pt^{2+} into the hexagonal channels of ***h*-WO$_3$** and ***h′*-WO$_3$**. H_2-TPR of fresh ***h*-PtWO$_3$** and ***h′*-PtWO$_3$** indicate a lower interaction of the Pt^{2+} cations with the ***h′*-WO$_3$** support compared to ***h*-WO$_3$**, resulting in the formation of bigger Pt particles when supported on ***h′*-WO$_3$**, as indicated by TEM and XPS. The CO oxidation TOFs were determined, and the reaction kinetics were studied. The greater CO oxidation TOF and the lower inhibiting effect of CO (CO reaction order) on the rate of CO catalytic oxidation for ***h′*-PtWO$_3$** compared to ***h*-PtWO$_3$** may be attributed to subtle changes in the electron density of the Pt nanoparticles, with a slightly higher electron density of these nanoparticles for the catalyst supported on h'-WO$_3$. Such a higher electron density of the h'-WO$_3$-supported Pt nanoparticles, which could only be detected by CO oxidation measurements, is ascribed to a greater extent of surface reduction for ***h′*-WO$_3$** as indicated by H_2-TPR and XPS. Therefore, CO oxidation kinetics appear as a unique tool to probe subtle changes in the electron density of supported Pt nanoparticles, information that could hardly be obtained by any other means. Finally, in contrast to h-WO$_3$, the recently discovered h'-WO$_3$ polymorph has the ability to accommodate a wide range of metal cation dopants into its structural framework. This study should then pave the way for a new family of materials that could not be achieved with traditional tungsten oxide polymorphs.

Supporting Information. Structural information obtained through Le Bail analysis of powder XRD patterns, TEM and STEM images of tungsten bronzes; Pt nanoparticles size study; H_2-TPR analysis of h'-WO$_3$ and h'-PtWO$_3$; CO oxidation and H_2 adsorption isotherms of Pt-SiO$_2$ and EELS W-$M_{4,5}$, Pt-$M_{4,5}$, and Cs-$M_{4,5}$ edges.

Corresponding Authors

José M. González-Calbet – *Departamento de Química Inorgánica, Facultad de Ciencias Químicas, Universidad Complutense, 28040 Madrid, Spain; ICTS ELECMI Centro Nacional de Microscopia Electrónica, Universidad Complutense, 28040 Madrid, Spain;* orcid.org/0000-0002-6481-6506; Email: jgcalbet@ucm.es

David Portehault – *Sorbonne Université, CNRS, Laboratoire Chimie de la Matière Condensée de Paris, LCMCP, F-75005 Paris, France;* orcid.org/0000-0003-4914-4913; Email: david.portehault@sorbonne-universite.fr

Authors

Isabel Gómez-Recio – *Sorbonne Université, CNRS, Laboratoire Chimie de la Matière Condensée de Paris, LCMCP, F-75005 Paris, France*

Cyril Thomas – *Sorbonne Université, CNRS, Laboratoire de Réactivité de Surface (LRS), F-75005 Paris, France*

Christophe Méthivier – *Sorbonne Université, CNRS, Laboratoire de Réactivité de Surface (LRS), F-75005 Paris, France*

María Luisa Ruiz-González – *Departamento de Química Inorgánica, Facultad de Ciencias Químicas, Universidad Complutense, 28040 Madrid, Spain*

Author Contributions

$^{\perp}$I.G.-R. and C.T. contributed equally.

■ ACKNOWLEDGMENTS

This project has received funding from the European Research Council (ERC) Consolidator Grant GENESIS under the European Union's Horizon 2020 research and innovation program (grant agreement no. 864850). The authors acknowledge the National Center for Electron Microscopy (ELECMI National Singular Scientific Facility) for access to corrected microscopy facilities. J.M.G.C. and M.L.R.G. acknowledge financial support to the Spanish Ministry of Science and Innovation through Research Project PID 2020-113753RB-100. C.T. thanks Sorbonne Université and CNRS for providing funding (Crédits récurrents) and access to the analytical equipment used at LRS in the present work. The authors also acknowledge the Fédération de Chimie et Matériaux de Paris-Center (FCMat, Fédération de Recherche 2482) for the access to the XPS facility. The crystal model of table of contents has been created by Rhodius software developed by J. A. Perez-Omil from the University of Cadiz (Spain).

■ REFERENCES

(1) Hai, Z.; Wei, Z.; Xue, C.; Xu, H.; Verpoort, F. Nanostructured Tungsten Oxide Thin Film Devices: From Optoelectronics and Ionics to Iontronics. *J. Mater. Chem. C* **2019**, *7* (42), 12968−12990.

(2) Besnardiere, J.; Ma, B.; Torres-Pardo, A.; Wallez, G.; Kabbour, H.; González-Calbet, J. M.; Von Bardeleben, H. J.; Fleury, B.; Buissette, V.; Sanchez, C.; Le Mercier, T.; Cassaignon, S.; Portehault, D. Structure and Electrochromism of Two-Dimensional Octahedral Molecular Sieve h'-WO_3. *Nat. Commun.* **2019**, *10* (1), No. 327.

(3) Chen, X.; Shen, Y.-F.; Suib, S. L.; O'Young, C. L. Characterization of Manganese Oxide Octahedral Molecular Sieve (M−OMS-2) Materials with Different Metal Cation Dopants. *Chem. Mater.* **2002**, *14* (2), 940−948.

(4) Mao, M.; Li, Y.; Hou, J.; Zeng, M.; Zhao, X. Extremely Efficient Full Solar Spectrum Light Driven Thermocatalytic Activity for the Oxidation of VOCs on OMS-2 Nanorod Catalyst. *Appl. Catal., B* **2015**, *174*−*175* (Supplement C), 496−503.

(5) Wang, Y.; Liu, M.; Li, K.; Zhang, A.; Guo, X. Crystallization Behavior of 3D-Structured OMS-2 under Hydrothermal Conditions. *CrystEngComm* **2015**, *17* (19), 3636−3644.

(6) Velty, A.; Corma, A. Advanced Zeolite and Ordered Mesoporous Silica-Based Catalysts for the Conversion of CO_2 to Chemicals and Fuels. *Chem. Soc. Rev.* **2023**, *52* (5), 1773−1946.

(7) Mattox, T. M.; Bergerud, A.; Agrawal, A.; Milliron, D. J. Influence of Shape on the Surface Plasmon Resonance of Tungsten Bronze Nanocrystals. *Chem. Mater.* **2014**, *26* (5), 1779−1784.

(8) Gao, T.; Jelle, B. P. Visible-Light-Driven Photochromism of Hexagonal Sodium Tungsten Bronze Nanorods. *J. Phys. Chem. C* **2013**, *117* (26), 13753−13761.

(9) Gu, Z.; Ma, Y.; Zhai, T.; Gao, B.; Yang, W.; Yao, J. A Simple Hydrothermal Method for the Large-Scale Synthesis of Single-Crystal Potassium Tungsten Bronze Nanowires. *Chem. - Eur. J.* **2006**, *12* (29), 7717−7723.

(10) Kaspera, W.; Zieliński, S.; Kotarba, A. Alkali Tungsten Bronzes as Soot Oxidation Catalysts: The Key Role of Electrodonor Properties of Catalytic Surface. *Catal. Commun.* **2017**, *98*, 76−80.

(11) Jin, S.; Gao, C.; Guo, J.; Fang, M.; Gao, Q.; Ren, X.; Chao, M.; Liang, E. Effects of Crystal Structure and Morphology on the Electrochromic Properties of Cs_xWO_3. *Solid State Ionics* **2022**, *385*, No. 116011.

(12) Portehault, D.; Gonell, F.; Gómez-Recio, I. Addressing Complex Transition Metal Oxides at the Nanoscale. In *Tailored Functional Oxide Nanomaterials. From Design to Multi-Purpose Applications*; Wiley-VCH GmbH, 2022; pp 43−88.

(13) Wang, H.; Zhang, L.; Zhou, Y.; Qiao, S.; Liu, X.; Wang, W. Photocatalytic CO_2 Reduction over Platinum Modified Hexagonal Tungsten Oxide: Effects of Platinum on Forward and Back Reactions. *Appl. Catal., B* **2020**, *263*, No. 118331.

(14) Runnerstrom, E. L.; Llordés, A.; Lounis, S. D.; Milliron, D. J. Nanostructured Electrochromic Smart Windows: Traditional Materials and NIR-Selective Plasmonic Nanocrystals. *Chem. Commun.* **2014**, *50* (73), 10555−10572.

(15) Zydlewski, B. Z.; Lu, H.-C.; Celio, H.; Milliron, D. J. Site-Selective Ion Intercalation Controls Spectral Response in Electrochromic Hexagonal Tungsten Oxide Nanocrystals. *J. Phys. Chem. C* **2022**, *126* (34), 14537−14546.

(16) Zeng, D.; Wang, H.; Zhu, X.; Cao, H.; Wang, W.; Zhang, Y.; Wang, J.; Zhang, L.; Wang, W. Photocatalytic Conversion of CO_2 to Acetic Acid by CuPt/WO_3: Chloride Enhanced C-C Coupling Mechanism. *Appl. Catal., B* **2023**, *323*, No. 122177.

(17) Doherty, R. P.; Krafft, J.-M.; Méthivier, C.; Casale, S.; Remita, H.; Louis, C.; Thomas, C. On the Promoting Effect of Au on CO Oxidation Kinetics of Au−Pt Bimetallic Nanoparticles Supported on SiO_2: An Electronic Effect? *J. Catal.* **2012**, *287*, 102−113.

(18) Bergeret, G.; Gallezor, P.; Ertl, G.; Knozinger, H.; Weitkamp, J. *Handbook of Heterogeneous Catalysis*; Wiley-VCH, 1997.

(19) Watanabe, M.; Okunishi, E.; Ishizuka, K. Analysis of Spectrum-Imaging Datsets in Atomic-Resolution Electron Microscopy. *Microsc. Anal.* **2009**, *23*, 5−7.

(20) Benson, J. E.; Hwang, H. S.; Boudart, M. Hydrogen-Oxygen Titration Method for the Measurement of Supported Palladium Surface Areas. *J. Catal.* **1973**, *30* (1), 146−153.

(21) Ji, Y.; van der Eerden, A. M. J.; Koot, V.; Kooyman, P. J.; Meeldijk, J. D.; Weckhuysen, B. M.; Koningsberger, D. C. Influence of Support Ionicity on the Hydrogen Chemisorption of Pt Particles Dispersed in Y Zeolite: Consequences for Pt Particle Size Determination Using the H/M Method. *J. Catal.* **2005**, *234* (2), 376−384.

(22) Oudenhuijzen, M. K.; van Bokhoven, J. A.; Ramaker, D. E.; Koningsberger, D. C. Theoretical Study on Pt Particle Adsorbate Bonding: Influence of Support Ionicity and Implications for Catalysis. *J. Phys. Chem. B* **2004**, *108* (52), 20247−20254.

(23) Wang, J.; Wang, Z.; Liu, C.-J. Enhanced Activity for CO Oxidation over WO_3 Nanolamella Supported Pt Catalyst. *ACS Appl. Mater. Interfaces* **2014**, *6* (15), 12860−12867.

(24) Greczynski, G.; Hultman, L. X-Ray Photoelectron Spectroscopy: Towards Reliable Binding Energy Referencing. *Prog. Mater. Sci.* **2020**, *107*, No. 100591.

(25) Scofield, J. H. Hartree-Slater Subshell Photoionization Cross-Sections at 1254 and 1487 EV. *J. Electron Spectrosc. Relat. Phenom.* **1976**, *8* (2), 129−137.

(26) Kozuch, S.; Martin, J. M. L. Turning Over" Definitions in Catalytic Cycles. *ACS Catal.* **2012**, *2* (12), 2787−2794.

(27) Shannon, R. D. Revised Effective Ionic Radii and Systematic Studies of Interatomic Distances in Halides and Chalcogenides. *Acta Crystallogr., Sect. A: Cryst. Phys., Diffr., Theor. Gen. Crystallogr.* **1976**, *32*, 751.

(28) Yang, H.; Sun, H.; Li, Q.; Li, P.; Song, K.; Song, B.; Wang, L. Structural, Electronic, Optical and Lattice Dynamic Properties of the Different WO_3 Phases: First-Principle Calculation. *Vacuum* **2019**, *164*, 411−420.

(29) Gerand, B.; Nowogrocki, G.; Guenot, J.; Figlarz, M. Structural Study of a New Hexagonal Form of Tungsten Trioxide. *J. Solid State Chem.* **1979**, *29* (3), 429−434.

(30) DePuccio, D. P.; Ruíz-Rodríguez, L.; Rodríguez-Castellón, E.; Botella, P.; López Nieto, J. M.; Landry, C. C. Investigating the Influence of Au Nanoparticles on Porous SiO_2−WO_3 and WO_3 Methanol Transformation Catalysts. *J. Phys. Chem. C* **2016**, *120* (49), 27954−27963.

(31) Alonso, F.; Riente, P.; Rodríguez-Reinoso, F.; Ruiz-Martínez, J.; Sepúlveda-Escribano, A.; Yus, M. Platinum Nanoparticles Supported on Titania as an Efficient Hydrogen-Transfer Catalyst. *J. Catal.* **2008**, *260* (1), 113−118.

(32) Salvati, L. J.; Makovsky, L. E.; Stencel, J. M.; Brown, F. R.; Hercules, D. M. Surface Spectroscopic Study of Tungsten-Alumina Catalysts Using x-Ray Photoelectron, Ion Scattering, and Raman Spectroscopies. *J. Phys. Chem. A* **1981**, *85* (24), 3700−3707.
(33) Bonnotte, T.; Doherty, R. P.; Sayag, C.; Krafft, J.-M.; Méthivier, C.; Sicard, M.; Ser, F.; Thomas, C. Insights into the WO_x Coverage-Dependent Location and Oxidation State of Noble Metals Supported on Tungstated Oxides: The Case of $Rh/WO_x-Ce_{0.62}Zr_{0.38}O_2$. *J. Phys. Chem. C* **2014**, *118* (14), 7386−7397.
(34) Kerkhof, F. P. J. M.; Moulijn, J. A. Quantitative Analysis of XPS Intensities for Supported Catalysts. *J. Phys. Chem. A* **1979**, *83* (12), 1612−1619.
(35) Cant, N. W.; Hicks, P. C.; Lennon, B. S. Steady-State Oxidation of Carbon Monoxide over Supported Noble Metals with Particular Reference to Platinum. *J. Catal.* **1978**, *54* (3), 372−383.
(36) Manuel, I.; Chaubet, J.; Thomas, C.; Colas, H.; Matthess, N.; Djéga-Mariadassou, G. Simulation of the Transient CO Oxidation over Rh^0/SiO_2 and $Rh^{x+}/Ce_{0.68}Zr_{0.32}O_2$ Catalysts. *J. Catal.* **2004**, *224* (2), 269−277.
(37) Bera, P.; Patil, K. C.; Jayaram, V.; Subbanna, G. N.; Hegde, M. S. Ionic Dispersion of Pt and Pd on CeO_2 by Combustion Method: Effect of Metal−Ceria Interaction on Catalytic Activities for NO Reduction and CO and Hydrocarbon Oxidation. *J. Catal.* **2000**, *196* (2), 293−301.

Supplementary information

Metal-support interactions in Pt-WO_3 heterostructures: role of WO_3 polymorphism

Isabel Gómez-Recio,[1] Cyril Thomas,[2] Christophe Méthivier,[2] María Luisa Ruiz-González,[3] José M. González-Calbet,[3,*] David Portehault,[1,*]

[1] Sorbonne Université, CNRS, Laboratoire Chimie de la Matière Condensée de Paris, LCMCP, 4 Place Jussieu, F-75005 Paris, France

[2] Sorbonne Université, CNRS, Laboratoire de Réactivité de Surface (LRS), 4 place Jussieu, F-75005, Paris, France

[3] Dpto. de Química Inorgánica I, Facultad de Ciencias Químicas, Universidad Complutense, 28040 Madrid, Spain

David Portehault: david.portehault@sorbonne-universite.fr

José M. González-Calbet: jgcalbet@ucm.es

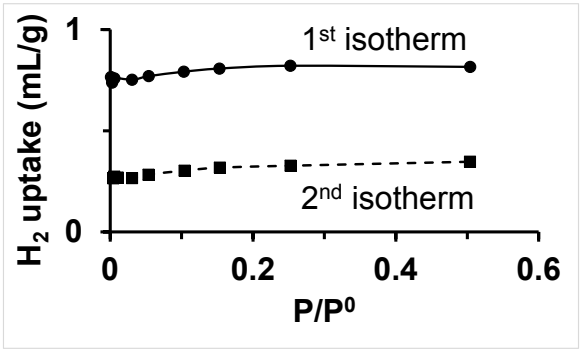

Figure S1. H_2 adsorption isotherms at 25 °C on Pt-SiO_2. First isotherm (●) and 2nd isotherm (■) performed after evacuation for 2 h at RT following the first isotherm.

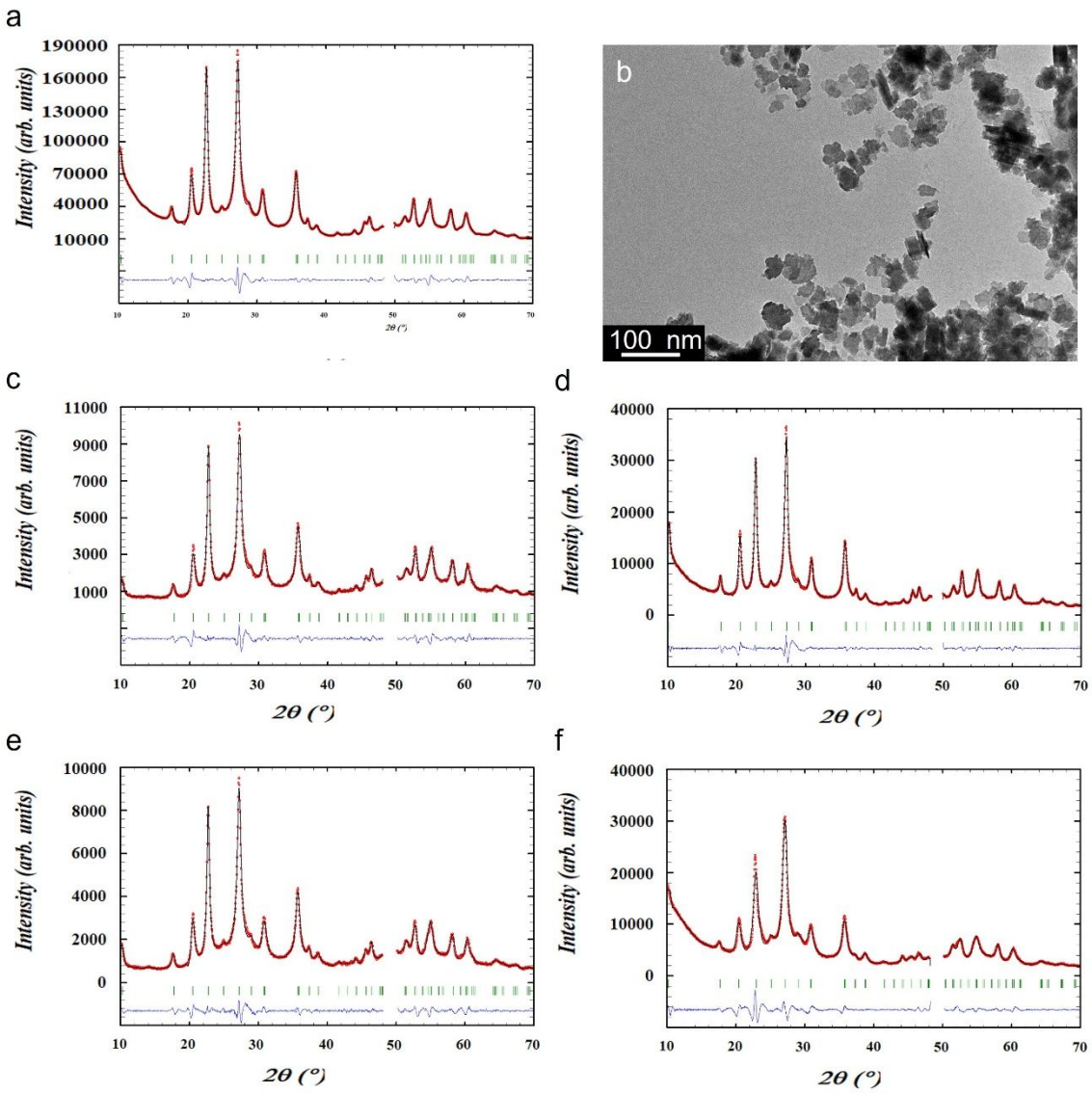

Figure S2. (a,c-f) Le Bail analysis of powder XRD patterns of hydrogen and Co, Cu, Pt and Cs doped bronzes, respectively. (b) Low magnification TEM image of the pristine hydrogen bronze *h'*-$H_{0.07}WO_3$.

Table S1. Cell parameters and crystallite size of hydrogen and doped bronzes provided by Le Bail analysis of XRD patterns (Figure S2).

	a (Å)	a (Å)	Chi^2	S_{Cryst} (nm)
***h'*-WO_3**	10.0116(4)	3.9234(2)	46.9	9.0 ± 1.1
***h'*-$CoWO_3$**	10.0128(4)	3.9169(2)	3.84	9.0 ± 1.2
***h'*-$CuWO_3$**	10.0195(3)	3.9077(1)	8.61	12.0 ± 2.5
***h'*-$PtWO_3$**	10.0138(4)	3.9132(2)	3.07	9.0 ± 1.2
***h'*-$CsWO_3$**	10.0443(6)	3.8837(3)	15.9	6.8 ± 1.6

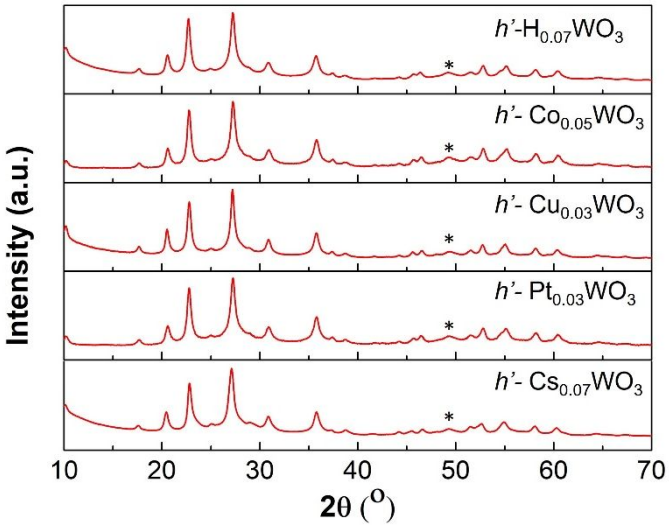

Figure S3. Powder XRD patterns of hydrogen and doped bronzes. Stars highlight a crystalline impurity, possibly a tungsten oxide.

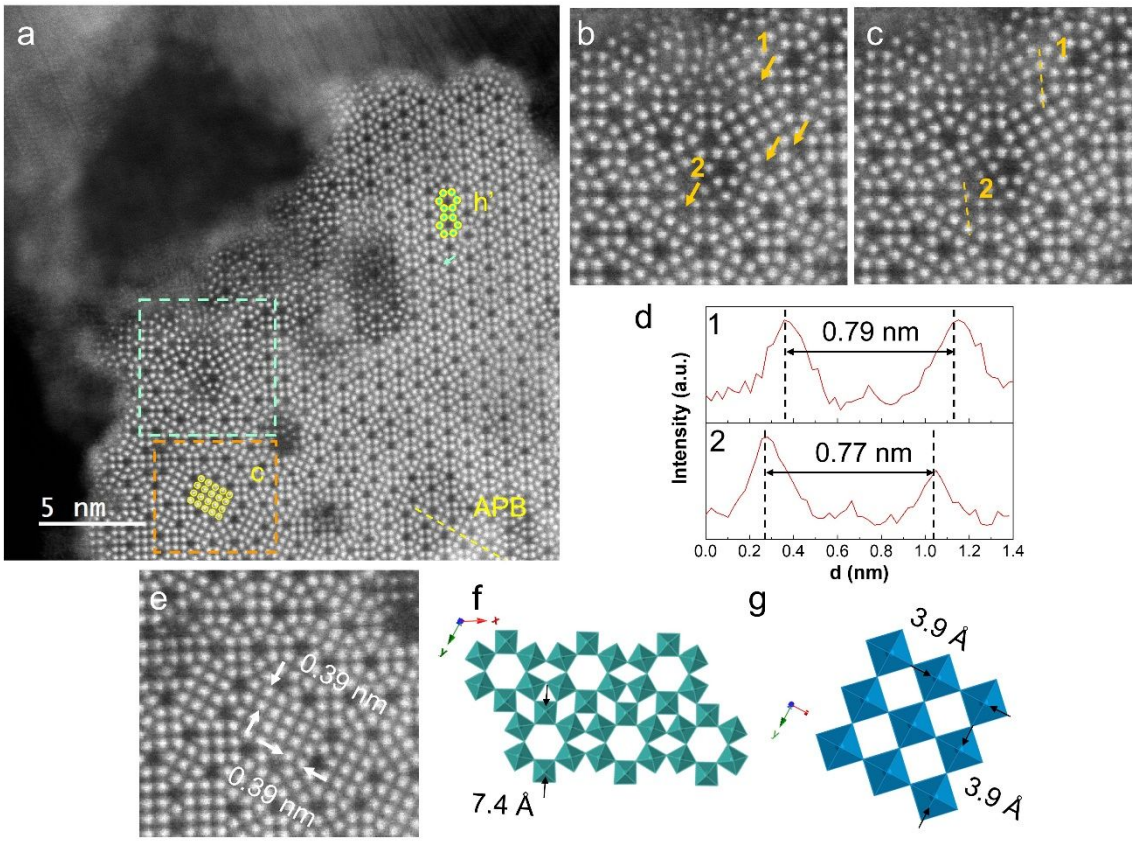

Figure S4 STEM study of ***h'*-PtWO$_3$**: **(a)** Atomically resolved HAADF image. Antiphase boundaries (APB) and *c*-WO_3 ("c") defects are outlined in comparison with regions without defects (*h'*). **(b, c)** Enlarged images of the green dashed region marked in (a). Orange arrows in (b) and (c) indicate contrast not observed in pristine ***h'*-H$_{0.07}$WO$_3$**.[1] **(d)** Intensity profile along the orange dashed lines in (c), positions where additional contrast are observed in (b). **(e)** Enlarged image of the orange dashed region marked in (a). Schemes of **(f)** the *h'*-WO_3 crystal structure of the bronze and **(g)** the *c*-WO_3 structure, oriented along the (001) direction.

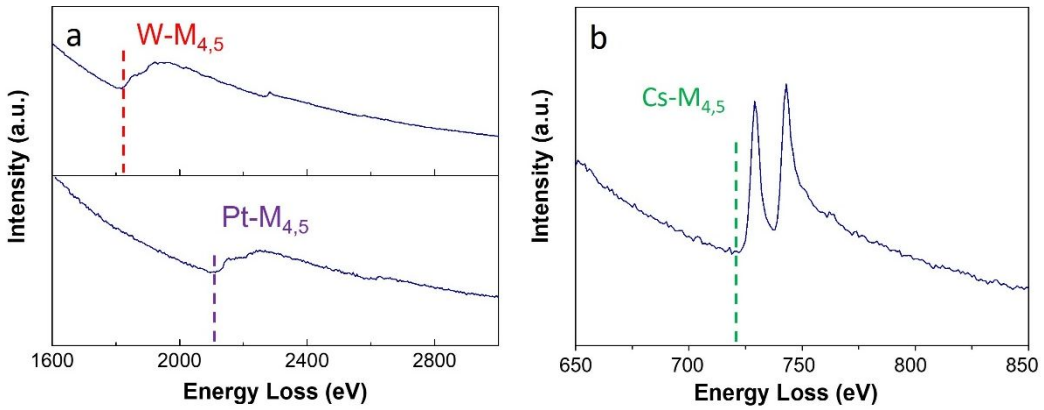

Figure S5. EELS W-$M_{4,5}$, Pt-$M_{4,5}$, and Cs-$M_{4,5}$ edges of metallic W, Pt, and CsI, from ref. [2]

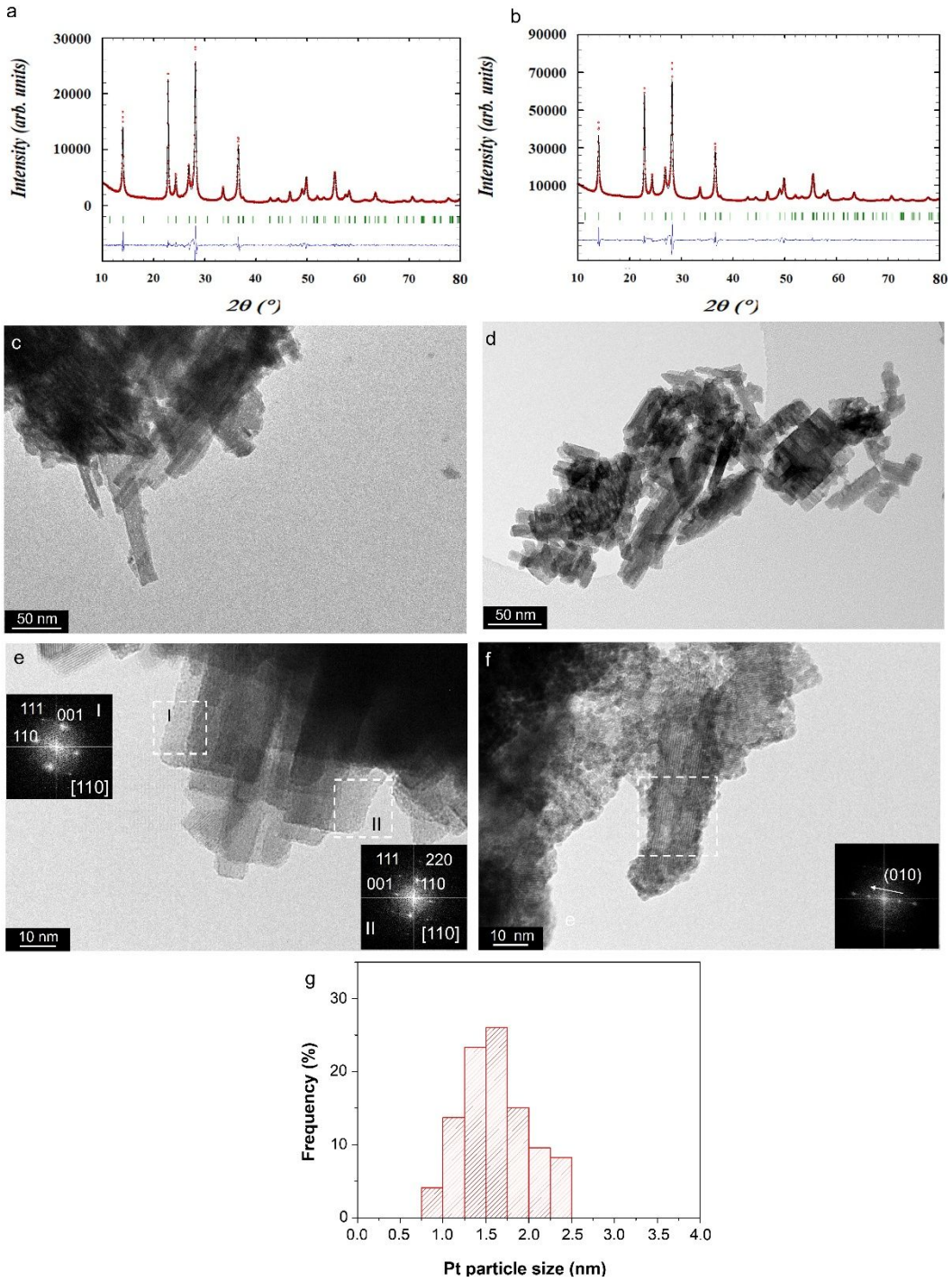

Figure S6. Le Bail analysis of powder XRD patterns of (a) pristine and (b) platinum doped *h*-WO_3. (c,d) Low and (e,f) high magnification TEM images of *h*-WO_3 and *h*-$Pt_{0.04}WO_3$, respectively. (g) Pt nanoparticles size distribution on *h*-$Pt_{0.04}WO_3$.

Table S2. Cell parameters and crystallite size of hydrogen and Pt doped bronzes provided by Le Bail analysis of XRD patterns (Figure S3).

	a (Å)	a (Å)	Chi^2	S_{Cryst} (nm)
***h*-WO_3**	7.3137(1)	7.7832(2)	9.01	23.4 ± 7.9
***h*-$PtWO_3$**	7.3114(1)	7.7841(2)	25	20.3 ± 7.2

Table S3. Average and volume-weighted particle size of platinum nanoparticles over ***h*-$PtWO_3$**.

	$\overline{d}\ (nm)$	$\overline{d_V}$ (nm)
Fresh *h*-$Pt_{0.04}WO_3$	1.6 ± 0.4	1.7 ± 0.4

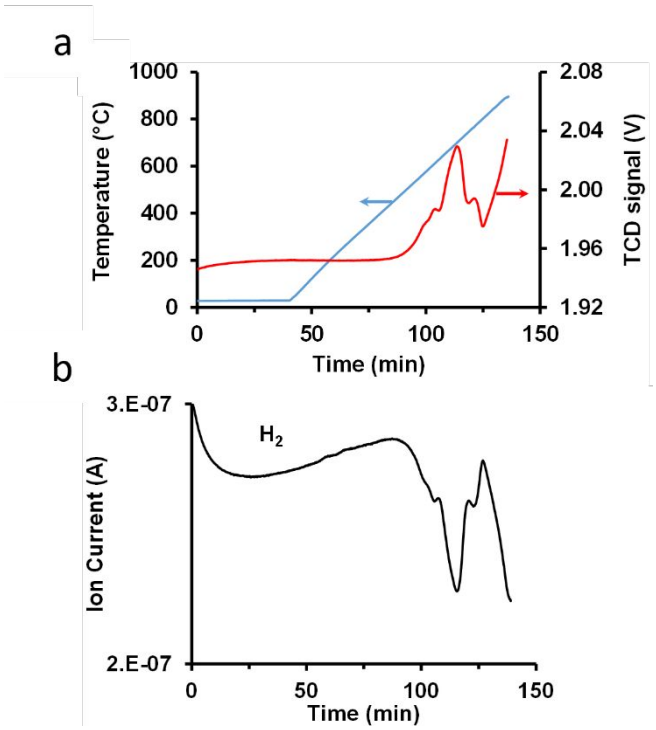

Figure S7. (a) Temperature and TCD traces, and (b) H_2 (M/Z = 2) trace recorded in the course of the H_2-TPR experiment carried out on 55.5 mg of ***h'*-WO_3**. The H_2-TPR experiments was carried out from RT to 900 °C (10 °C min^{-1}) under 25 mL min^{-1} H_2(5%)/Ar.

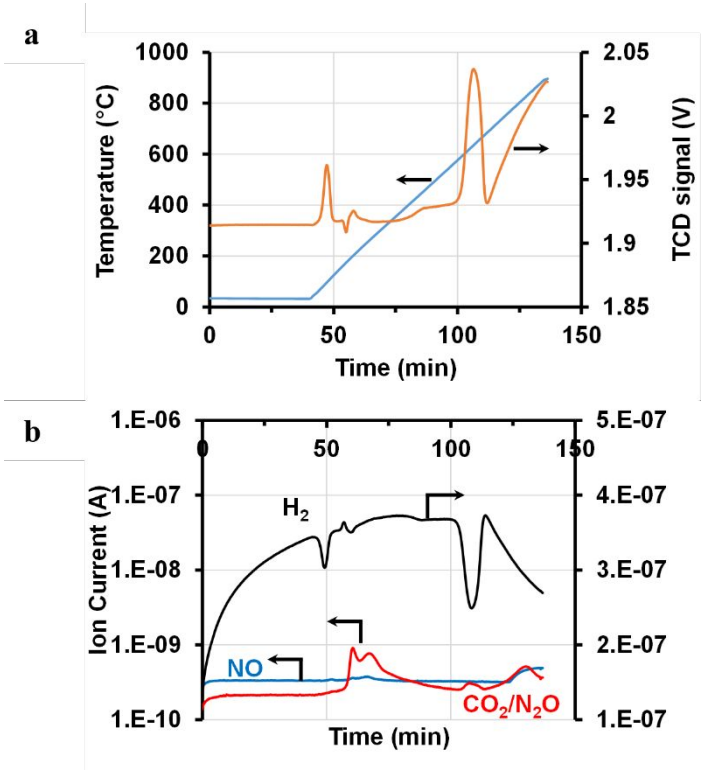

Figure S8. (a) Temperature and TCD traces, and (b) H_2 (M/Z = 2, black), NO (M/Z = 30, blue) and CO_2/N_2O (M/Z = 44, red) traces recorded in the course of the H_2-TPR experiment carried out on 57.0 mg of ***h'*-PtWO$_3$**. The H_2-TPR experiment was carried out from RT to 900 °C (10 °C min^{-1}) under 25 mL min^{-1} H_2(5%)/Ar.

CO oxidation on Pt-SiO$_2$

After reduction under H_2 at 300 °C for 30 minutes, the Pt-SiO_2 sample diluted in SiO_2 was submitted to a CO(1%)-O_2(1%)-He light-off experiment when increasing the reaction temperature up to about 250 °C (**Figure S9a**, orange trace). Then, the temperature of the reactor was decreased and the CO conversion recorded (**Figure S9a**, grey trace). Finally, the CO conversion was recorded from 160 to 240 °C under steady-state conditions (**Figure S6a**, blue trace). CO conversions measured under steady-state and when ramping up the temperature are in good agreement, whereas those measured when decreasing the reaction temperature are slightly higher than the previous ones. This difference may be attributed to a lower CO coverage in the case of the transient experiment ran by decreasing the temperature compared to the two other measurements. Using the steady-state measurements recorded from 180 to 200 °C (**Figure S9a**, blue trace), the apparent activation energy of the CO oxidation reaction was estimated to 86 kJ mol^{-1} (**Figure S9b**, blue trace), in good agreement with the apparent activation energy determined under transient conditions when increasing the reaction temperature from 160 to 210 °C (90 kJ mol^{-1}, **Figure S9b**, orange trace). The CO and O_2 reaction orders measured at 190 °C amounted to about -0.37

(**Figure S9c**) and 0.84 (**Figure S9d**), respectively. Such reaction orders are in agreement with those reported earlier by Cant *et al.*[3] on a similar sample.

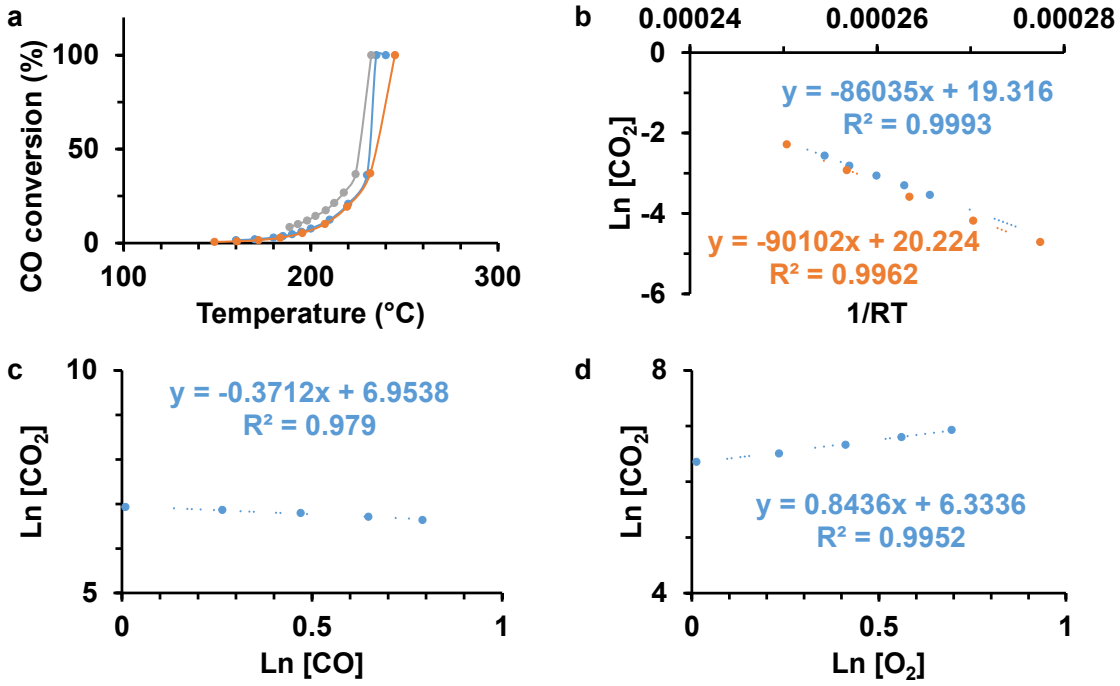

Figure S9. Data recorded on 32.8 mg of **Pt-SiO$_2$** diluted in 400 mg of SiO_2 for the catalytic oxidation of CO by O_2 with a total flow rate of 100 mL/min, **(a)** temperature transient CO(1.0 %)-O_2(1.0 %)-He reactions with increasing reaction temperature at 3 °C min^{-1} (orange), decreasing reaction temperature (grey) and under steady-state conditions (blue), **(b)** apparent activation energies (E_a) determined from about 180 to 200 °C from the data reported in (a, blue trace) and from 160 to 210 °C from the data reported in (a, orange trace), **(c)** CO reaction order determined at 190 °C with an O_2 concentration of 2.0 % and CO concentrations varying from 1.0 to 2.2 %. **(d)** O_2 reaction order determined at 190 °C with a CO concentration of 1.0 % and O_2 concentrations varying from about 1.0 to 2.0 %. The reaction orders were estimated in lean mixtures (excess of oxygen compared to stoichiometry).

The TOF measured at 200 °C on **Pt-SiO$_2$** (0.02 s^{-1}) is also lower than that reported by Bera *et al.* over a Pt-Al_2O_3 catalyst (0.13 s^{-1}),[4] although the origin of the reported TOF is unclear. Indeed, considering the reported reaction rate of 12.92 µmol g^{-1} and full dispersion of 1 wt. % Pt on Al_2O_3, the TOF should be 0.25 s^{-1} at 200 °C. If one considers Pt particles of about 7 nm according to the authors with a Pt dispersion of 16 %,[5] the TOF would be 1.58 s^{-1}, which is much higher than the TOF we measured for the **Pt-SiO$_2$** sample.

(1) Besnardiere, J.; Ma, B.; Torres-Pardo, A.; Wallez, G.; Kabbour, H.; González-Calbet, J. M.; Von Bardeleben, H. J.; Fleury, B.; Buissette, V.; Sanchez, C.; Le Mercier, T.; Cassaignon, S.; Portehault, D. Structure and Electrochromism of Two-Dimensional Octahedral Molecular Sieve h'-WO_3. *Nat. Commun.* **2019**, *10* (1), 327. https://doi.org/10.1038/s41467-018-07774-x.

(2) Ahn, C. C.; Krivanek, O. L.; Burgner, R. P.; Disko, M. M.; Swann, P. R. EELS Atlas : A Reference Collection of Electron Energy Loss Spectra Covering All Stable Elements; Gatan, Inc., Warrendale, Pa., 1983.

(3) Cant, N. W.; Hicks, P. C.; Lennon, B. S. Steady-State Oxidation of Carbon Monoxide over Supported Noble Metals with Particular Reference to Platinum. *J. Catal.* **1978**, *54* (3), 372–383. https://doi.org/https://doi.org/10.1016/0021-9517(78)90085-4.

(4) Bera, P.; Patil, K. C.; Jayaram, V.; Subbanna, G. N.; Hegde, M. S. Ionic Dispersion of Pt and Pd on CeO_2 by Combustion Method: Effect of Metal–Ceria Interaction on Catalytic Activities for NO Reduction and CO and Hydrocarbon Oxidation. J. Catal. 2000, 196 (2), 293–301. https://doi.org/https://doi.org/10.1006/jcat.2000.3048.

(5) Bergeret, G.; Gallezor, P.; Ertl, G.; Knozinger, H.; Weitkamp, J. Handbook of Heterogeneous Catalysis; Wiley-VCH, 1997.